The Astrophysical Journal Supplement Series, 218:1 (29pp), 2015 May doi:10.1088/0067-0049/218/1/1

THE BOLOCAM GALACTIC PLANE SURVEY. XI. TEMPERATURES AND SUBSTRUCTURE OF GALACTIC CLUMPS BASED ON 350 μM OBSERVATIONS

Manuel Merello[1,2], Neal J. Evans II[1], Yancy L. Shirley[3], Erik Rosolowsky[4], Adam Ginsburg[5], John Bally[6], Cara Battersby[7], and Michael M. Dunham[7]
[1] The University of Texas at Austin, Department of Astronomy, 2515 Speedway, Stop C1400, Austin, TX 78712-1205, USA; manuel@astro.as.utexas.edu
[2] Istituto di Astrofisica e Planetologia Spaziali-INAF, Via Fosso del Cavaliere 100, I-00133 Roma, Italy
[3] Steward Observatory, University of Arizona, 933 North Cherry Avenue, Tucson, AZ 85721, USA
[4] Department of Physics, 4-181 CCIS, University of Alberta, Edmonton, AB T6G 2E1, Canada
[5] European Southern Observatory, ESO Headquarters, Karl-Schwarzschild-Strasse 2, D-95748 Garching bei Munchen, Germany
[6] CASA, University of Colorado, 389-UCB, Boulder, CO 80309, USA
[7] Harvard-Smithsonian Center for Astrophysics, 60 Garden Street, MS 78, Cambridge, MA 02138, USA
Received 2014 May 15; accepted 2015 January 8; published 2015 May 1

ABSTRACT

We present 107 maps of continuum emission at 350 μm from Galactic molecular clumps. Observed sources were mainly selected from the Bolocam Galactic Plane Survey (BGPS) catalog, with three additional maps covering star-forming regions in the outer Galaxy. The higher resolution of the SHARC-II images (8.″5 beam) compared with the 1.1 mm images from BGPS (33″ beam) allowed us to identify a large population of smaller substructures within the clumps. A catalog is presented for the 1386 sources extracted from the 350 μm maps. The color temperature distribution of clumps based on the two wavelengths has a median of 13.3 K and mean of 16.3 $\pm$ 0.4 K, assuming an opacity law index of 1.7. For the structures with good determination of color temperatures, the mean ratio of gas temperature, determined from NH_3 observations, to dust color temperature is 0.88 and the median ratio is 0.76. About half the clumps have more than 2 substructures and 22 clumps have more than 10. The fraction of the mass in dense substructures seen at 350 μm compared to the mass of their parental clump is ~0.19, and the surface densities of these substructures are, on average, 2.2 times those seen in the clumps identified at 1.1 mm. For a well-characterized sample, 88 structures (31%) exceed a surface density of 0.2 g cm^{-2}, and 18 (6%) exceed 1.0 g cm^{-2}, thresholds for massive star formation suggested by theorists.

Key words: catalogs – dust, extinction – Galaxy: structure – stars: formation – submillimeter: ISM – surveys

Supporting material: extended figure, figure set, machine-readable tables

1. INTRODUCTION

Although high-mass stars play a key role in the structure and evolution of our Galaxy, there are still many questions that need to be answered before we have a paradigm for their formation process (Stahler et al. 2000; Bally & Zinnecker 2005; Zinnecker & Yorke 2007; Tan et al. 2014). Adopting the nomenclature of Williams et al. (2000), star clusters form in dense clumps ($M \sim 50 - 500\ M_\odot$, sizes ~0.3 − 3 pc) of giant molecular clouds while individual stars form in cores ($M \sim 0.5 - 5\ M_\odot$, sizes ~0.03 − 0.2 pc). An important step in the observational study of massive star formation is the identification and characterization of clumps and their resolution into cores. Studies of compact structures in our Galaxy will give fundamental "ground truth" for the analysis of nearby galaxies where individual clumps and cores cannot be resolved and will provide source information for observations of the Milky Way with a new generation of instruments, such as the Atacama Large Millimeter/Submillimeter Array.

There are complementary approaches to the study of massive star-forming regions. We may consider obtaining molecular line observations, which are a good diagnostic of line of sight motions in a cloud, but variations in tracer abundances due to depletion and complex chemical processing, excitation conditions and the impacts of radiation fields and shocks add uncertainties (Evans 1999). We may also proceed by mapping the continuum emission toward these sources. Newly formed stars heat the dust of their parental molecular cores and this dust emits in the far-infrared and submillimeter wavelengths (Garay & Lizano 1999). Continuum emission observations at (sub)millimeter wavelengths offer a reliable tracer of the column density and clump masses due to the low optical depth of the dust (e.g., Johnstone & Bally 2006), and they have made an increasingly significant contribution to the understanding of star formation. Reddening and extinction of starlight also provide a measure of column densities (Bohlin et al. 1978), and mid-IR large scale surveys have identified dark patches obscuring the bright background, which are associated with dense molecular gas (e.g., Egan et al. 1998; Simon et al. 2006). Studies of the physical properties of these regions, called Infrared Dark Clouds, suggest they are the birthplaces of high-mass stars and stellar clusters (e.g., Rathborne et al. 2006, 2010; Battersby et al. 2010). In addition, near-infrared extended emission has also been considered a tracer of the column density of dense dark clouds, interpreted as scattered ambient starlight observed from the outer parts of dense cores ("cloudshine," e.g., Foster & Goodman 2006; Padoan et al. 2006).

Several studies have made progress toward the characterization of massive star-forming regions, but they are usually biased because target selection required existing signposts of newly formed high-mass stars, including maser emission, far-infrared emission, or the presence of HII regions (Churchwell et al. 1990; Cesaroni et al. 1991; Plume et al. 1992). Therefore, the identification of clumps with a less biased survey will improve our understanding of the early stages of massive stars. Examples include large scale surveys of particular regions, such as the study of the W3 giant molecular cloud with

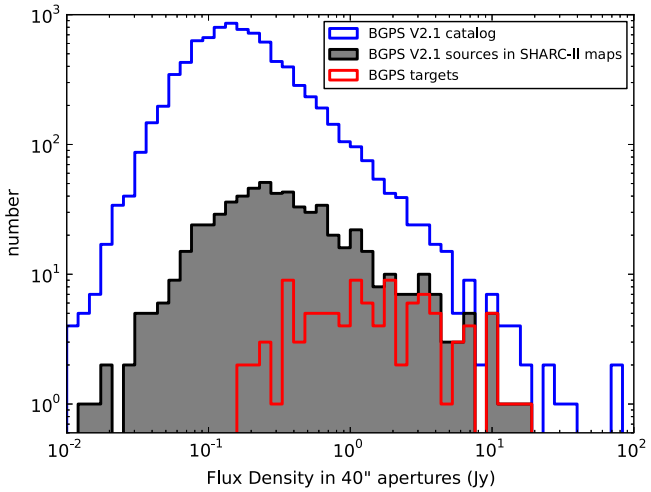

Figure 1. Distribution of 40″ aperture flux density of the complete sample of 8594 sources from the BGPS V2.1 catalog (blue line), along with those 619 sources contained in the SHARC-II maps (shaded black line). The red line shows the distribution of the 104 sources considered as representative targets (see Section 2.1).

SCUBA by Moore et al. (2007) or the Cygnus-X molecular cloud complex region with MAMBO receiver by Motte et al. (2007). Large-scale blind surveys of the Galactic plane at far-IR, submm, and mm wavelengths have recently been completed. The ATLASGAL survey mapped the southern part of the plane at 870 μm using the 12m APEX telescope (Schuller 2009; Contreras et al. 2013). Spaceborne missions, such as *WISE* (Wright et al. 2010), *Spitzer*/GLIMPSE (Benjamin et al. 2003), and MIPSGAL (Carey et al. 2009) have mapped most of the Galactic plane at a resolution of a few to 10″, at wavelengths between 3.6 and 24 μm. The *Herschel*/Hi-GAL survey (Molinari et al. 2010) covered the entire Galactic plane with resolutions between 5″ and 36″, in five bands at 70, 160, 250, 350 and 500 μm. In addition, the 15 m James Clerk Maxwell Telescope is using SCUBA-2 850 and 450 μm emission to map the Galactic plane and several nearby Gould Belt clouds. These surveys have provided a robust tracer of dust properties (column density and mean grain temperature), for different phases of the interstellar medium.

The Bolocam Galactic Plane Survey (BGPS; Aguirre et al. 2011) is one of the first ground-based surveys to map the continuum emission at 1.1 mm over a large region of the northern Galactic plane. The BGPS coverage region extended from $l = -10°$ to +86.°5 for $b = \pm 0.°5$, at a resolution of ∼30″, and it identified 8454 compact sources throughout the Galaxy (Rosolowsky et al. 2010). Depending on their distance, millimeter features may be cores, clumps, or clouds (McKee & Ostriker 2007), although BGPS sources are mostly clumps (Dunham et al. 2011). An improved reduction and a new version (V2.0) of the BGPS maps and catalog was released (Ginsburg et al. 2013), including an additional ∼20 square degree coverage area in the third and fourth quadrant, and ∼2 square degree in the first quadrant. This new reduction shows an improved flux calibration with respect to the former version (V1.0), in agreement with other data surveys on the Galaxy. The characterization of the angular transfer function of the Bolocam pipeline shows that the flux recovery is above 90% for scales between 33″ and 80″, with a steep drop for scales above ∼100″. While version 2.0 of the catalog contains 8559 sources, 35 sources were unintentionally excluded, and they were added in a new version (V2.1), for a total of 8594 sources. Figure 1 shows the distribution of 40″ aperture flux density of V2.1 sources. Although the basic statistical properties of the catalogs remain unaltered, there are some effects on the source extraction when considering the new map versions with improved quality. Comparing the source extraction in the V1.0 and V2.1 overlap region, V2.1 recovers fewer compact sources (8004), with only ∼70% of those having a clear V1.0 match, and these are considered more reliable and stable identified sources (see Figure 10 in Ginsburg et al. 2013). Figures 11 and 12 in Ginsburg et al. (2013) show visual examples of the lost sources, which are generally small sources on the shoulders of bright ones that have now been included in the bright source in the catalog.

We selected a sample of sources from the BGPS catalog, initially from V1.0 and later from V2.1, toward the most crowded and brightest portions of the Galactic plane including the Galactic center, the Molecular Ring near $l = 30°$, and Cygnus-X, and used the Submillimeter High Angular Resolution Camera II (SHARC-II; Dowell 2003) to obtain continuum maps of them.at 350 μm. The high resolution of the SHARC-II observations (FWHM beam size of 8.″5) is in particular very useful when we observe small structures at great distances in the Galaxy, and the comparison of flux densities of sources at 350 μm and 1.1 mm will give us constraints on their dust temperatures, hence improving the determination of masses and column densities of the molecular clumps.

SHARC-II has been used before for studying low-mass dense cores from the *Spitzer* Legacy Program "From Molecular Cores to Planet-Formation Disks" (Wu et al. 2007; A. Suresh et al. 2015, in preparation), concluding that observations with this instrument are better to distinguish between starless and protostellar cores than observations at longer wavelengths. While Mueller et al. (2002) studied dense clumps selected for having massive star formation using SHARC at 350 μm, there has not been a comprehensive study of BGPS-selected sources with SHARC-II. A recent study by Ragan et al. (2013) shows how ground-based observations at 350 μm continuum emission of regions of high-mass and cluster formation can give information on substructures within them. For a set of 11 nearby infrared-dark clouds (IRDCs), they obtained data on 350 μm continuum emission with the SABOCA instrument at the APEX telescope, finding a large population of small core-like structures. Higher resolution observations at submm wavelengths allow the study of the complex process of massive star formation from fragmentation of molecular clumps to individual substructures, such as cold and hot cores.

We present a set of 107 continuum emission maps at 350 μm obtained with SHARC-II. These include 104 maps of clump-like BGPS V2.1 sources and 3 maps of outer Galaxy sources not included in the catalog. This paper is organized as follows. Section 2 describes the selection of targets from the BGPS catalog and the SHARC-II instrument. Section 3 describes the data reduction and calibration methods for our set of submm continuum maps. Section 4 presents the results of the extraction of sources in the images, including source recovery tests, a catalog of these sources, the procedure for association between sources in the 350 μm maps and the 1.1 mm sources, and the comparison between SHARC-II and *Herschel* at 350 μm. Section 5 describes the determination of color temperatures for BGPS sources found in our set of maps, comparing them with temperature determination from spectral energy distribution

(SED) fitting from Hi-GAL and other continuum surveys. Correlations between our dust temperature estimations and high-density molecular tracers are also presented. In Section 6 we explore consequences from our results for mass and surface density estimations of millimeter sources. In Section 7, we present conclusions from our analysis.

2. OBSERVATIONS

Observations were taken in several runs between 2006 June and 2012 September at the Caltech Submillimeter Observatory (CSO[8]). The observations required excellent weather conditions, with a measured optical depth at 225 GHz ranging between 0.030 and 0.094 (measured at zenith position), with an average value of $\tau_{225\ \mathrm{GHz}} = 0.057$, corresponding to an optical depth at 350 μm (857 GHz) of $\tau_{350\,\mu\mathrm{m}} = 1.41$. In general, we observed our targets when they were culminating, and we avoided observing sources below an elevation of 30° or above 80°.

2.1. Target Selection

The targets were initially selected from sources in the BGPS V1.0 catalog. We chose sources with strong emission at 1.1 mm (typically with peak emission above 1 Jy beam^{-1}) toward densely populated regions, many of them known as active star-forming regions, such as the Galactic center, $l = 30°$, Cygnus-X region, W3 and W5 molecular clouds, GemOB1 region, and others. Several of those targets were extended and they were likely to have unresolved substructure at a resolution of 30″ Most of the time the observation fields were centered directly on a V1.0 source, but in some cases we tried to cover several sources in the same field. Starting in 2009 December, we added to our list of targets bright sources selected from new Bolocam maps that were later incorporated in BGPS V2.0. Considering that almost all targets from V1.0 catalog are incorporated in V2.1 (Ginsburg et al. 2013), we consider the latest version of the catalog for our analysis. In just one of our maps, L136.52 +1.24, there are three sources marginally detected in V1.0 but not included in subsequent V2.0 or V2.1 catalog versions. We also obtained 350 μm maps of the outer Galaxy star-forming regions SH2-209, SH2-307, and *IRAS* 03233+5833 (e.g., Klein et al. 2005; Richards et al. 2012), which were not covered by the BGPS survey. The maps of these regions are L151.61–0.24, L234.57+0.82, and L142.01+1.77, respectively. These observations are included for completeness, but they are not included in analysis that requires BGPS data.

For a better characterization of our targets with respect to the complete catalog, we consider the brightest V2.1 source in each map as the representative target for that map. In some cases, where adjacent maps share the brightest source, we consider the second brightest source as a representative target. From the 104 maps at 350 μm with BGPS sources, we then have a subsample of V2.1 sources considered as representative targets. Figure 1 shows in red the distribution of flux density in 40″ apertures for our sample of 104 representative targets. The distribution has an average of 2.63 Jy and a median of 1.37 Jy, much higher than the values for the overall BGPS catalog. However, weaker sources were covered in the same fields, so the final flux density distribution of BGPS sources with 350 μm data is closer to that of the full catalog (see black line in Figure 1). We found a total of 619 V2.1 sources in our sample of SHARC-II maps, with an average and median flux density of 0.79 Jy and 0.29 Jy, respectively, about twice the values for the complete V2.1 catalog (average of 0.35 Jy and median of 0.16 Jy for 40″ apertures).

2.2. Instrument and Observational Method

SHARC-II is a background-limited facility camera operating at 350 μm or 450 μm, located at the CSO on Mauna Kea, HI. It consists of a 32×12 array of doped silicon "pop-up" bolometers and it has a mean beam size of 8.″5 at 350 μm. The array has a full size of 2.′59 × 0.′97, which makes the instrument start to lose sensitivity to emission on scales larger than ∼1′. We used the box scan mode of SHARC-II without chopping[9] for mapping regions with sizes significantly larger than the size of the array. In the box scan mode, the scan pattern moves across the rectangular field of view (FOV), starting in the center of the array and going straight until the edge of the bounding box, where it changes trajectory emulating the bounce of a ball on a billiard table. The advantage of this scan mode is that it provides better isolation against 1/*f* noise, with more uniformly distributed noise across the FOV in comparison with the alternative sweep mode with Lissajous scan pattern. Different box sizes were used in our data acquisition, between $2.'5 \times 2.'5$ and $18' \times 18'$, although the bulk of our observations were obtained with $10' \times 10'$ boxes. Column 3 in Table 2 shows the size for each map.

For all our observations we used the Dish Surface Optimization System (DSOS)[10] to correct the dish-surface figure for imperfections and gravitational deformations as the dish moves in elevation during observations.

3. DATA REDUCTION AND CALIBRATION

3.1. Data Reduction

The 350 μm raw data were reduced using the Comprehensive Reduction Utility for SHARC-II (CRUSH; Kovács 2006). CRUSH is a Java-based software which solves a series of iterative models, attempting to reproduce atmospheric and instrumental effects on the observations, removing the sky emission common to all bolometers at first order (e.g., Beelen et al. 2006). We used version 2.10 of CRUSH, publicly accessible from the CSO webpage.

Figure 2 shows an example of the error or noise maps that reduction with CRUSH produces for each observed region. In general, all SHARC-II maps are much noisier toward the edges by a factor of ∼4 with respect to the measured average noise of the image. At a distance of ∼20″ (twice the beam size) from the edge, the noise is only increased by a factor of ∼2. Also, when taking multiple scans for a single map at different runs, the orientation of the FOV rotates, and the regions that do not overlap in the integration of the source show a significant increase in the noise. The rest of the map shows some residuals of the pattern used in the box scan mode, but in general the inner parts of these maps are well represented by uniform noise.

[8] The CSO was operated by the California Institute of Technology, until 2013 March 31 under cooperative agreement with the National Science Foundation (AST-0838261).

[9] See http://submm.caltech.edu/∼sharc/

[10] See http://cso.caltech.edu/dsos/DSOS_MLeong.html

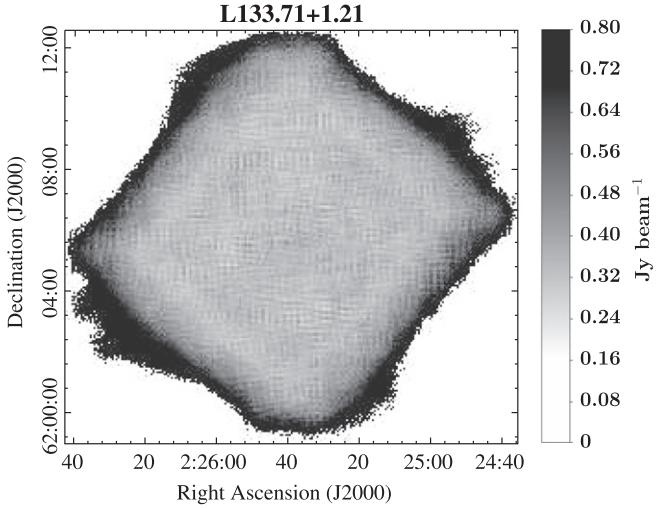

Figure 2. Error map obtained from CRUSH reduction for L133.71+1.21. The image unit is Jy beam^{-1} (beam size of 8.5″). The measured average noise for the L133.71+1.21 map is 0.338 Jy beam^{-1}. The average noise for the complete sample of maps is 744 mJy beam^{-1}.

3.2. Calibration

The maps were reduced in instrumental units of μV, and we estimated the flux conversion factors C_θ in order to measure the flux densities of the sources in units of Jy. On our analysis, we followed the same method used on SHARC-II maps by Wu et al. (2007) and on SCUBA maps by Shirley et al. (2000), based on aperture calibrations over a given angular size θ. Flux estimations obtained from aperture corrected photometry are less sensitive to uncertainties due to effects of sidelobes. The observed flux density for an aperture of diameter θ is $S_\nu(\lambda, \theta) = C_\theta\, V(\lambda, \theta)$, with $V(\lambda, \theta)$ the voltage measured at wavelength λ in an aperture of diameter θ. We used the fluxes from Mars, Uranus, and Neptune to obtain the flux conversion factors for two different apertures, 20″ and 40″. We restricted our flux estimation to 40″ considering the limited sensitivity of the instrument to large scale emission. The bulk of the compact structures identified on the maps have sizes below this limit.

To compare the 350 μm data with the 1.1 mm images from BGPS survey, we also convolved the 350 μm to match the 33″ FWHM beam from Bolocam. Therefore, we also estimated the flux conversion factor $C_{40}^{33''}$ for an aperture of 40″ using the images of the calibration sources convolved to a 33″ beam. The flux densities of sources and calibrators in instrumental units were measured using Starlink's *aperadd* package.

In addition, we estimated the flux conversion factor for one beam, $C_{\rm beam}$, which we used to express the peak flux of each source and the 1 σ rms of the maps in units Jy beam^{-1}. $C_{\rm beam}$ is obtained from the integrated flux density of the calibrators in one beam and the peak pixel of the map in instrument units. We then have an average value for the conversion μV to Jy pixel^{-1} = 32.23 Jy beam^{-1}, for the beam size and pixel scale of the instrument. Therefore, the value of C_θ will depend of the number of pixels considered. From the maps, the average value of $C_{\rm beam}$ = 8.27 Jy beam^{-1} μV^{-1}, and then

$$\begin{aligned} 1 \text{ Jy beam}^{-1} &= 503.8 \text{ MJy ster}^{-1} \\ &= 0.031 \text{ Jy pixel}^{-1} \\ &= 0.121\ \mu\text{V}^{-1}. \end{aligned}$$

Table 1
Average Calibration Factors

Date	$C_{\rm beam}$ (Jy beam^{-1} μV^{-1})	C_{20} (Jy μ V^{-1})	C_{40} (Jy μV^{-1})	$C_{40}^{33''}$ (Jy μV^{-1})
2006 Jun	9.84 ± 0.68	0.35 ± 0.03	0.28 ± 0.02	0.42 ± 0.03
2007 Jul	7.01 ± 0.21	0.23 ± 0.01	0.20 ± 0.01	0.29 ± 0.01
2007 Oct	8.08 ± 0.32	0.27 ± 0.01	0.23 ± 0.01	0.34 ± 0.01
2009 Sep	6.05 ± 0.25	0.21 ± 0.02	0.17 ± 0.01	0.26 ± 0.02
2009 Dec	5.89 ± 0.11	0.22 ± 0.01	0.17 ± 0.01	0.25 ± 0.01
2010 Jul[a]	7.31 ± 0.25	0.24 ± 0.01	0.20 ± 0.01	0.30 ± 0.01
2010 Jul 24	17.83 ± 2.50	0.67 ± 0.06	0.51 ± 0.06	0.77 ± 0.09
2010 Dec	6.69 ± 0.16	0.23 ± 0.01	0.19 ± 0.01	0.28 ± 0.01
2011 Dec	10.82 ± 0.39	0.38 ± 0.01	0.31 ± 0.01	0.46 ± 0.02
2012 Sep	15.59 ± 0.85	0.52 ± 0.03	0.43 ± 0.02	0.65 ± 0.04

[a] Does not include calibration from 2010 July 24.

For the calibration of the images, only the observations of planets were considered. While the secondary calibrators mentioned in Section 4.1 are useful to check the pointing when planets are not available, they are not as bright and their flux densities are not as well known as planets. Therefore, we avoided using them to minimize uncertainties in the estimation of calibration factors.

Table 6 in the Appendix section gives the observation dates (column 1), the planet observed (column 2), the observed opacity at 225 GHz at that date (column 3), the computed values of $C_{\rm beam}$ (column 4), and C_θ at different apertures (columns 5 and 6). Column 7 gives the calibration factor for an aperture of 40″ obtained for the planet images convolved to a beam of 33″. Table 1 shows the average values of C_θ for the different observation epochs. According to these results, the uncertainties in the calibration of the maps are between 15-20%, consistent with previous observations and calibration estimations for the SHARC-II instrument (Wu et al. 2007).

While some sources may have significant contributions to the broad-band flux density from line emission, it is usually a small fraction of the dust continuum emission (e.g., Groesbeck 1995). The continuum flux measured with SHARC-II (780–910GHz for the 350 μm filter) could in principle be contaminated by the CO(7 − 6) line. Hatchell & Dunham (2009) estimated a contribution less than 100 mJy beam^{-1} in the SHARC-II 350 μm band for a CO(7 − 6) integrated intensity of 100 K km s^{-1}, which is smaller than the typical sensitivity found in our maps, and they considered that the CO line may contribute ∼20% of the continuum emission in the 350 μm band. We adopted that limit in this work as a conservative value for possible line contamination.

4. RESULTS

4.1. Map Description

Figure 3 shows as an example the 350 μm continuum map of L133.71+1.21, corresponding to the W3 Main region (see

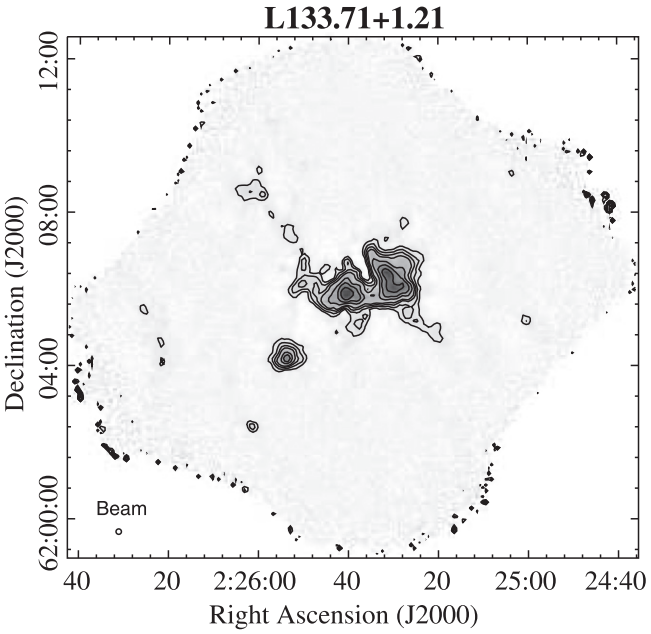

Figure 3. Map at 350 μm obtained with SHARC-II toward L133.71+1.21, corresponding to the W3 Main star-forming region. Beam size of image is shown in the bottom left corner. Contour levels represent 3σ, 6σ, 10σ ,15σ, 30σ, 50σ and 100σ, with a rms noise σ = 338 mJy beam^{-1}.

Megeath et al. 2008; Rivera-Ingraham et al. 2013, and references therein). Besides the two bright infrared sources IRS5 and IRS4 (Wynn-Williams et al. 1972), the small beam size of the 350 μm maps allows us to identify several sources near them, and some elongated, filamentary-like structures and scattered faint sources. These types of features are found recurrently in the 350 μm maps and we characterize their correspondence with 1.1 mm sources later in Section 4.5.

We obtained a total sample of 107 maps, with an average noise of 744 mJy beam^{-1}, and a standard deviation of 443 mJy beam^{-1}. These maps are presented in Figure 25 in the Appendix. The complete sample of maps will be available from IPAC.[11] Because the noise increases at the edges of the images (see Section 3.1), we estimated a more representative value of the mean rms of each map on a region toward the central area. In the 10′ × 10′ maps, the considered area has a diameter of 7′. Column 7 in Table 2 shows the representative rms noise of each map. The average 1σ noise value estimated this way is 478 mJy beam^{-1}, with a median of 375 mJy beam^{-1} and a standard deviation of 298 mJy beam^{-1}. Each map has an angular scale of 1.618 arcsec per pixel. Table 2 lists, for each map observed, the configuration used, the size and center of each map, the date on which the map was taken, and the 1 σ noise of the map in units of mJy beam^{-1}. Integration time was obtained in blocks of ∼14 minutes. The pointing was checked on planets such as Mars, Uranus, and Neptune, and with secondary objects when the planets were not available, such as *IRAS*16293-2422, K350, G34.3, W75N and CRL 618. The blind pointing uncertainty varied between 1.″8 and 2.″1 for azimuth and between 0.″8 and 1.″6 for zenith angle.

[11] http://irsa.ipac.caltech.edu/data/BOLOCAM_GPS/

4.2. Source Extraction

To facilitate comparison with the BGPS sources, we used the same algorithm for source extraction as was used for the BGPS catalogs, *Bolocat* (Rosolowsky et al. 2010). *Bolocat* identifies sources based on their significance with respect to the local estimate of the noise in a map, subdividing regions with high significance into individual sources based on local maxima inside that region. Each pixel is assigned to an individual source using a seeded watershed, in a similar way to other source extraction algorithms (*Clumpfind*, Williams et al. 1994; *SExtractor*, Bertin & Arnouts 1996). The source identification process is determined by three parameters: $P_{\rm amp}$, the amplitude of the signal compared to a local estimation of the noise σ (noise estimation, as α, δ); $P_{\rm base}$, the base level of emission at which the identified region is expanded; and the deblending parameter $P_{\rm deb}$, used in decomposing regions of emission with multiple local maxima. First, *Bolocat* masks all data above $P_{\rm amp}$ of a particular image, and extends a region to include all connected regions of emission above $P_{\rm base} = 1\sigma(\alpha, \delta)$ since areas with marginal significance adjacent to regions of emission are probably real. Second, each identified region is examined and subdivided according to the level of contrast between local maxima. For each pair of local maxima in a region, the amplitudes of emission, I_1 and I_2, are compared with the highest contour of emission containing the local maxima pair, $I_{\rm crit}$, and if any I_1 or I_2 is less than $P_{\rm deb}$ above $I_{\rm crit}$, that local maximum is discarded as a subregion. *Bolocat* also avoids recovering sources (and sub-sources from the deblending process) with sizes less than the beam FWHM. A detailed description of the algorithm is presented in Rosolowsky et al. (2010). BGPS catalogs V1.0 and V2.1 used as parameters for the extraction of sources $P_{\rm amp} = 2\sigma(l, b)$, $P_{base} = 1\sigma(l, b)$ and $P_{\rm deb} = 0.5\sigma(l, b)$, with $\sigma(l, b)$ the local noise estimation, as a function of Galactic coordinates, on the BGPS maps.

We tested *Bolocat* in the SHARC-II maps varying the $P_{\rm amp}$, P_{base} and $P_{\rm deb}$ parameters, checking which of them reproduce a "by eye" extraction of sources in those maps. Using the same parameters as BGPS, spurious low brightness sources were recovered across the maps, with several of them toward the noisy edges of the maps, and bright extended sources are subdivided until the routine reaches small areas, comparable to the beam size of the maps. Better results were obtained considering $P_{\rm amp} = 3\sigma(\alpha, \delta)$, $P_{base} = 1\sigma(\alpha, \delta)$ and $P_{\rm deb} = 1\sigma(\alpha, \delta)$, and these values were used for all maps (inclusive those outside the BGPS coverage) and the following catalog of BPGS substructures at 350 μm.

Figure 4 shows an example of one SHARC-II map and the corresponding image at 1.1 mm obtained from BGPS. The angular scales of SHARC-II and BGPS images are 1.6 and 7.2 arcsec per pixel, respectively. The better angular resolution of SHARC-II reveals substructures within the clumps identified by the BGPS catalog. Crowded fields and extended clumps identified at 1.1 mm show small components and filaments when they are observed at 8.″5 resolution.

4.3. Source Recovery Experiments

We performed similar tests to the ones done for BGPS to assess catalog properties compared with the real distribution of emission on the sky. For these tests, we inserted sources in selected maps that do not have detected sources, or that have

Table 2
Observing Information

Map	Config[a]	Size	Map Center		Obs. Date	1 σ Noise[b]
			R.A. (J2000)	Decl. (J2000)		(mJy beam^{-1})
L359.85+0.00[c]	A	10′ × 10′	17:45:15.356	−29:03:48.64	2006 Jun	994
L000.00+0.00[c]	A	10′ × 10′	17:45:38.222	−28:56:15.83	2006 Jun	1453
L000.15+0.00[c]	A	10′ × 10′	17:45:59.055	−28:48:38.10	2006 Jun	1438
L000.30+0.00[c]	A	10′ × 10′	17:46:20.056	−28:40:51.99	2006 Jun	1086
L029.95-0.05	A	10′ × 10′	18:46:10.078	−02:40:45.19	2006 Jun	514
L030.00+0.00	A	10′ × 10′	18:46:05.764	−02:36:40.25	2006 Jun	462
L030.15+0.00	A	10′ × 10′	18:46:21.926	−02:28:41.39	2006 Jun	426
L030.30+0.00	A	10′ × 10′	18:46:38.373	−02:20:39.29	2006 Jun	496
L030.45+0.00	A	10′ × 10′	18:46:54.711	−02:12:38.81	2006 Jun	603
L030.60+0.00	A	10′ × 10′	18:47:11.158	−02:04:35.09	2006 Jun	888
L030.70-0.07	A	10′ × 10′	18:47:36.576	−02:01:32.42	2006 Jun	510
L030.80-0.05	A	10′ × 10′	18:47:43.784	−01:55:09.17	2006 Jun	529
L030.88+0.13	A	10′ × 10′	18:47:13.872	−01:45:57.32	2006 Jun	367
L034.26+0.15	A	10′ × 10′	18:53:19.759	+01:14:36.57	2006 Jun	395
L076.16+0.09	A	10′ × 10′	20:23:52.185	+37:36:41.20	2006 Jun	249
L077.93+0.02	A	10′ × 10′	20:29:23.675	+39:00:58.88	2006 Jun	389
L078.14-0.32	A	10′ × 10′	20:31:26.817	+38:58:53.21	2006 Jun	408
L078.96+0.37	A	10′ × 10′	20:31:03.924	+40:02:54.24	2006 Jun	445
L079.28+0.30	A	10′ × 10′	20:32:20.042	+40:15:45.21	2006 Jun	558
L080.92-0.11	A	10′ × 10′	20:39:16.364	+41:19:41.83	2006 Jun	724
L081.45+0.04	A	10′ × 10′	20:40:23.200	+41:50:33.25	2006 Jun	274
L081.68+0.54	A	10′ × 10′	20:39:01.659	+42:19:37.11	2006 Jun	802
L082.55+0.14	A	10′ × 10′	20:43:35.922	+42:46:07.20	2006 Jun	255
L075.76+0.41	A	10′ × 10′	20:21:24.076	+37:27:55.95	2007 Jul	652
L076.12-0.24	B	6′ × 6′	20:25:07.547	+37:23:14.34	2007 Jul	388
L076.35-0.58	B	6′ × 6′	20:27:10.982	+37:22:29.34	2007 Jul	430
L078.92-0.19	A	10′ × 10′	20:33:18.191	+39:41:24.34	2007 Jul	689
L078.17-0.31	A	10′ × 10′	20:31:29.785	+39:00:20.75	2007 Jul	800
L079.62+0.49	A	10′ × 10′	20:32:36.698	+40:39:16.34	2007 Jul	1489
L079.11-0.35	A	10′ × 10′	20:34:33.491	+39:44:46.95	2007 Jul	1226
L080.86+0.38	A	10′ × 10′	20:37:00.649	+41:34:35.34	2007 Jul	1874
L110.11+0.05	C	4′ × 4′	23:05:11.371	+60:14:41.67	2007 Oct	288
L111.62+0.38	C	4′ × 4′	23:15:32.196	+61:07:30.77	2007 Oct	342
L134.28+0.86	C	4′ × 4′	02:29:02.834	+61:33:28.83	2007 Oct	275
L134.83+1.31	C	4′ × 4′	02:34:45.364	+61:46:15.77	2007 Oct	296
L136.38+2.27	C	4′ × 4′	02:50:08.515	+61:59:54.27	2007 Oct	257
L136.83+1.07	C	4′ × 4′	02:49:04.352	+60:43:23.95	2007 Oct	250
L111.28-0.66	A	10′ × 10′	23:16:04.681	+60:02:06.00	2009 Sep–2009 Dec	286
L111.54+0.78	A	10′ × 10′	23:13:44.302	+61:28:10.18	2009 Sep	496
L133.71+1.21	A	10′ × 10′	02:25:41.066	+62:05:42.68	2009 Sep–2009 Dec	338
L133.95+1.06	A	10′ × 10′	02:27:03.912	+61:52:14.05	2009 Sep–2009 Dec	338
L111.26-0.77	A	10′ × 10′	23:16:11.144	+59:55:27.74	2009 Dec	538
L111.78+0.59	A	10′ × 10′	23:16:13.500	+61:22:51.01	2009 Dec	412
L111.79+0.71	D,A	10′ × 10′	23:15:52.220	+61:30:02.26	2009 Dec–2012 Sep	307
L111.88+0.82	D,A	10′ × 10′	23:16:15.419	+61:37:42.69	2009 Dec	473
L136.52+1.24	D	10′ × 10′	02:47:25.531	+61:00:34.20	2009 Dec	260
L136.85+1.14	E	3′ × 3′	02:49:28.155	+60:47:02.96	2009 Dec	337
L136.95+1.09	D	10′ × 10′	02:50:02.727	+60:41:52.32	2009 Dec	475
L137.69+1.46	H	11′ × 11′	02:56:47.527	+60:41:21.90	2009 Dec	667
L138.30+1.56	D,A	10′ × 10′	03:01:34.013	+60:29:10.72	2009 Dec–2011 Dec–2012 Sep	205
L138.48+1.63	D,A	10′ × 10′	03:03:09.052	+60:27:39.61	2009 Dec–2011 Dec–2012 Sep	266
L173.14+2.36	A	10′ × 10′	05:37:57.556	+36:00:18.63	2009 Dec	777
L173.17+2.35	G	4′ × 4′	05:37:59.420	+35:58:27.54	2009 Dec	320
L173.47+2.43	F	2.5′ × 2.5′	05:39:07.589	+35:46:02.82	2009 Dec	487
L173.57+2.44	F	2.5′ × 2.5′	05:39:24.823	+35:40:55.71	2009 Dec	421
L173.62+2.81	D	10′ × 10′	05:41:07.430	+35:50:21.17	2009 Dec	359
L173.72+2.70	G	4′ × 4′	05:40:52.684	+35:41:45.31	2009 Dec	387
L173.76+2.67	G	4′ × 4′	05:40:51.995	+35:38:53.79	2009 Dec	301
L188.79+1.03	A	10′ × 10′	06:09:06.309	+21:50:45.79	2009 Dec	259
L188.95+0.88	D,A	10′ × 10′	06:08:52.987	+21:38:19.76	2009 Dec	268
L189.03+0.78	D,A	10′ × 10′	06:08:39.856	+21:31:11.38	2009 Dec	290
L189.12+0.64	A	10′ × 10′	06:08:20.114	+21:22:04.54	2009 Dec	403
L189.68+0.19	D,A	10′ × 10′	06:07:47.653	+20:39:28.06	2009 Dec	155

Table 2
(Continued)

Map	Config[a]	Size	Map Center		Obs. Date	1 σ Noise[b]
			R.A. (J2000)	Decl. (J2000)		(mJy beam^{-1})
L189.85+0.39	I	18′ × 18′	06:08:53.475	+20:36:24.00	2009 Dec	505
L190.17+0.74	A	10′ × 10′	06:10:51.620	+20:29:49.63	2009 Dec	184
L192.60-0.16	D	10′ × 10′	06:12:28.348	+17:56:17.12	2009 Dec	340
L192.60-0.05	D,A	10′ × 10′	06:12:53.279	+17:59:28.55	2009 Dec–2010 Dec	271
L192.72+0.04	A	10′ × 10′	06:13:28.147	+17:55:38.60	2009 Dec	335
L192.81+0.11	D	10′ × 10′	06:13:55.135	+17:53:09.02	2009 Dec	328
L192.98+0.14	D	10′ × 10′	06:14:21.502	+17:45:02.52	2009 Dec	383
L196.42-1.66	A	10′ × 10′	06:14:36.606	+13:52:04.40	2009 Dec	470
L203.23+2.06	A	10′ × 10′	06:41:00.779	+09:33:56.58	2009 Dec	269
L203.35+2.03	A	10′ × 10′	06:41:07.741	+09:26:52.53	2009 Dec	314
L213.71-12.62	D	10′ × 10′	06:07:42.663	−06:23:27.15	2009 Dec	421
L217.37-0.07	A	10′ × 10′	06:59:17.374	−03:59:14.04	2009 Dec	704
L234.57+0.82	D	10′ × 10′	07:35:28.482	−18:45:34.36	2009 Dec	1051
L001.10-0.07	A	10′ × 10′	17:48:28.655	−28:01:44.77	2010 Jul	849
L023.31-0.26	A	10′ × 10′	18:34:39.947	−08:40:36.21	2010 Jul	379
L023.43-0.22	A	10′ × 10′	18:34:45.046	−08:32:55.27	2010 Jul	375
L024.50-0.08	A	10′ × 10′	18:36:14.747	−07:31:49.77	2010 Jul	306
L024.65-0.13	A	10′ × 10′	18:36:44.447	−07:25:23.71	2010 Jul	357
L024.78+0.12	A	10′ × 10′	18:36:04.446	−07:11:28.75	2010 Jul	363
L025.40-0.18	A	10′ × 10′	18:38:16.246	−06:47:09.20	2010 Jul	482
L030.61+0.16	A	10′ × 10′	18:46:39.147	−01:59:36.24	2010 Jul	349
L031.28+0.05	A	10′ × 10′	18:48:14.651	−01:26:51.80	2010 Jul	303
L081.11-0.16	A	10′ × 10′	20:40:05.498	+41:26:56.24	2010 Jul	341
L081.28+1.01	A	10′ × 10′	20:35:39.600	+42:17:38.79	2010 Jul	250
L081.39+0.73	A	10′ × 10′	20:37:12.963	+42:12:38.77	2010 Jul	341
L081.48+0.00	A	10′ × 10′	20:40:37.896	+41:50:26.77	2010 Jul	353
L081.76+0.60	A	10′ × 10′	20:39:01.567	+42:25:36.73	2010 Jul	329
L031.41+0.31	A	10′ × 10′	18:47:34.152	−01:12:46.30	2010 Jul 24	791
L081.88+0.77	A	10′ × 10′	20:38:39.559	+42:37:37.68	2010 Jul 24	717
L183.40-0.58	A	10′ × 10′	05:51:16.720	+25:43:32.50	2010 Dec	255
L189.78+0.33	A	10′ × 10′	06:08:32.990	+20:38:33.34	2010 Dec	294
L202.58+2.42	A	10′ × 10′	06:41:06.051	+10:18:59.80	2010 Dec	370
L142.01+1.77	A	10′ × 10′	03:27:29.910	+58:43:55.31	2011 Dec	305
L151.61-0.24	A	10′ × 10′	04:11:07.205	+51:09:21.54	2011 Dec	266
L154.37+2.58	A	10′ × 10′	04:36:18.153	+51:11:02.11	2011 Dec	266
L169.18-0.89	A	10′ × 10′	05:13:26.754	+37:27:38.75	2011 Dec	232
L172.88+2.27	A	10′ × 10′	05:36:53.085	+36:10:29.56	2011 Dec	315
L211.53-19.27	A	10′ × 10′	05:39:57.873	−07:27:48.36	2011 Dec	254
L111.42+0.76	A	10′ × 10′	23:12:52.873	+61:24:31.27	2012 Sep	375
L111.88+0.99	A	10′ × 10′	23:15:45.489	+61:47:37.40	2012 Sep	226
L134.20+0.75	A	10′ × 10′	02:28:05.671	+61:29:25.54	2012 Sep	525
L189.85+0.50	A	10′ × 10′	06:09:19.407	+20:39:39.18	2012 Sep	506
L189.94+0.34	A	10′ × 10′	06:08:53.761	+20:30:07.72	2012 Sep	590
L206.60-16.37	A	10′ × 10′	05:41:47.488	−01:57:59.97	2012 Sep	563

[a] A: BOX SCAN 571.429 600 40.0 45. B: BOX SCAN 345.600 360 30.0 45. C: BOX SCAN 228.571 240 20.0 45. D: BOX SCAN 606.1 636.4 60.0 45. E: BOX SCAN 169.7 167.5 60.0 45. F: BOX SCAN 144.6 148.0 60.0 45. G: BOX SCAN 144.6 148.0 60.0 45. H: BOX SCAN 707.1 669.9 60.0 45. I: BOX SCAN 1060.7 1157.1 60.0 45. The configuration BOX SCAN X Y R A indicates that the map has a size of X(arcsec) × Y(arcsec), a scan rate R (arcsec/s), and a scanning angle A (deg).

[b] Representative noise is estimated on the central area of each map, avoiding edges (see Section 4.1).

[c] Additional SHARC-II 350 μm continuum data on the Galactic center were presented by Bally et al. (2010).

just a couple of compact identified sources. The selected maps are those of L030.15+0.00 (2 identified sources), L078.92–0.19 (0), L079.62+0.49 (0), L079.11–0.35 (1), L080.86+0.38 (2), L111.26–0.77 (2), L111.79+0.71 (0), L136.52+1.24 (2), and L137.69+1.46 (0). The median rms noise of these maps is 667 mJy beam^{-1}, larger than 83% of the estimated noise in the whole set of maps. This set of maps will be considered as a conservative representation of an emission free SHARC-II map. For those maps that already have identified sources, we flagged the detection of those sources and any input sources near them, and therefore the recovered properties of input sources will not be affected by the emission prior to the test. After the artificial Gaussian objects were added, the maps were reduced in the same standard way as the rest of the SHARC-II maps. Although Gaussian brightness profiles do not quite represent all structures observed in the 350 μm maps, they are still good models of compact sources. Thus, the bulk of sources will be well represented in these tests.

We examined the degree of completeness of the catalog of substructures at different flux density limits. For the nine test

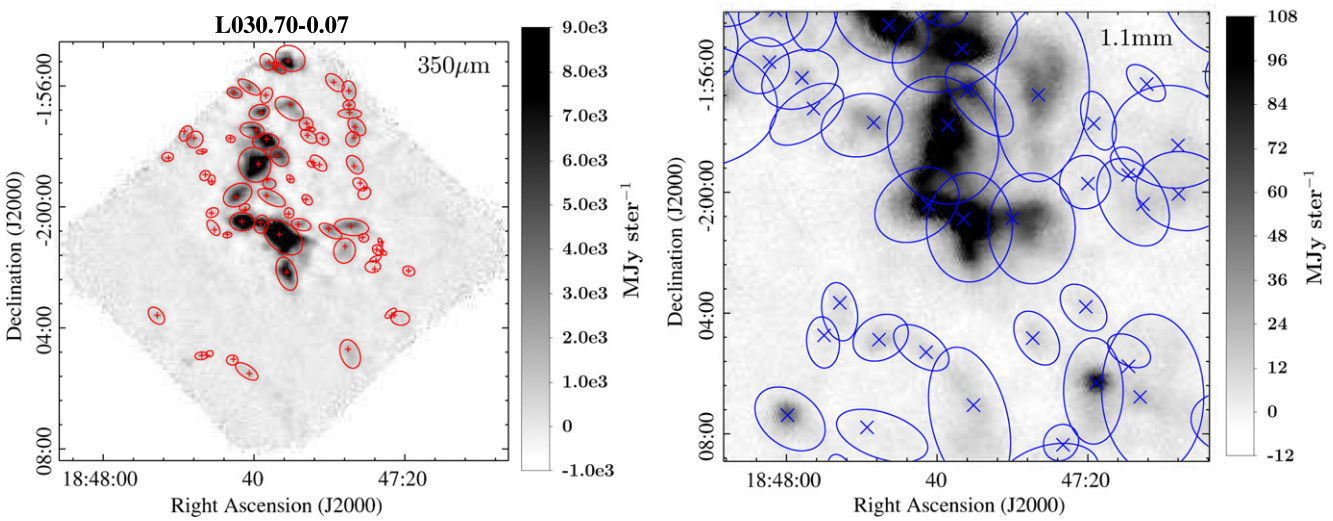

Figure 4. Example of the extraction of sources with *Bolocat*. Left: map of L030.70-0.07 with SHARC-II at 350 μm (FWHM beam of 8.″5). Right: the same region mapped with Bolocam at 1.1 mm (FWHM beam of 33″). Some structures of Bolocam have several substructures mapped at the better resolution of SHARC-II. Also, the figure shows BGPS sources with no counterpart in the 350 μm map(see Section 4.2 for a description of *Bolocat* parameters used on the extraction of sources).

maps, we input sources with an FWHM of 9″ and amplitudes uniformly ranging between $0.1\sigma_{\rm rms}$ and $15\sigma_{\rm rms}$, with $\sigma_{\rm rms}$ the noise of each map. For $\sigma_{\rm rms} = 667$ mJy beam^{-1}, this range corresponds to sources with flux densities between 0.19 Jy to 28.5 Jy. Taking into account that the edges of the maps have a larger noise than the central area of the map with uniform noise, we consider the detection fraction of sources across the whole map, and sources inside a central area of 7′ in diameter. Figure 5 shows the results of the test of completeness. The vertical lines represent 1 to 6 times the average $\sigma_{\rm rms}$ value of the complete set of SHARC-II maps. For sources inside the central area of the map, the detection is >99% complete at the $6\sigma_{\rm rms}$ level. For sources with amplitude less than $3\sigma_{\rm rms}$, the detection fraction is less than 15%. For the rest of our test, we only considered sources inside a central area of radius 3.5′ to avoid noisy edge effects.

The next test we performed was examining the properties recovered by the extracting algorithm for a distribution of input sources. We compared input and extracted flux densities for objects with FWHM equal to 23″ (2.7 times the beam size of the 350 μm maps). Initially, we tested the flux recovery of artificial sources on apertures of 20″ and 40″, and the total integrated flux, in units of μV. The integrated flux is estimated from the area of significant emission defined by the watershed extraction. At an aperture smaller than the source size, we only recovered part of the total intensity as expected, and the flux recovery at a larger aperture as 40″ is almost equivalent to the integrated flux. All the sources extracted in our catalog have a recovered flux density less than 3000 μV (∼300 Jy). Figure 6 shows results of this flux recovery test. For the integrated emission, calibration was done using the $C_{\rm beam}$ conversion factor, and flux recovery at 20″ and 40″ was calibrated using C_{20} and C_{40}, respectively. The image indicates that the 40″ aperture flux density could be underestimating the amount of flux recovered for input sources, with a difference with respect to the curve of the integrated flux of ∼10%. That difference between integrated and aperture flux density recovery gets bigger for input sources with larger size. For example, for input sources with FWHM equal to four times the

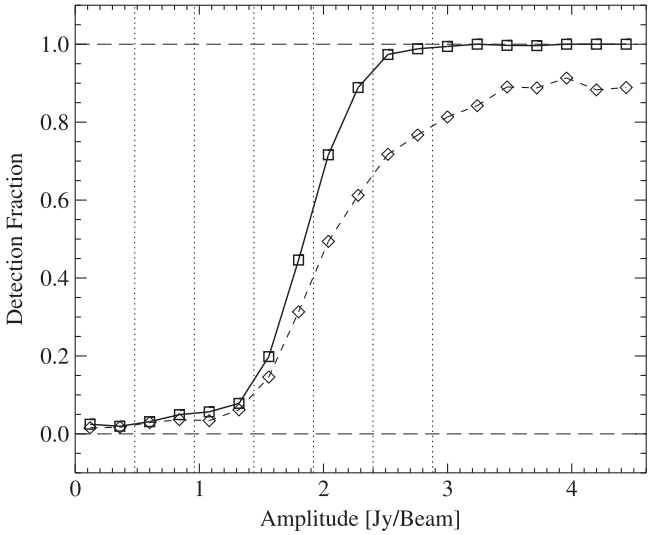

Figure 5. Completeness fraction derived from fake source tests. The tests were performed in nine SHARC-II maps with different noise levels. The plot shows the results of those detections scaled to the mean noise of the catalog maps (0.48 Jy beam^{-1}). The fraction of sources recovered is plotted as a function of input source intensity. The vertical dotted lines indicate $\{1, 2, 3, 4, 5, 6\}\sigma$. The dashed line with diamonds corresponds to fake sources across the whole map, while the continuous line with squares corresponds to sources at a distance <3.′5 from the center of the map. The results indicate that the catalog is complete at the >99% limit for sources with flux densities >6σ.

beam size (∼30″), the difference between a 40″ aperture and the integrated flux is around 35%.

The size recovered with *Bolocat* for input sources with a peak signal of $50\sigma_{\rm rms}$ is shown in Figure 7. The sizes of small sources are well recovered by the algorithm, but they become underestimated for sources larger than ∼60″ These results are similar to those found in the BGPS maps, where the radii of recovered sources become underestimated for radii ⩾200″ The largest source that we found in the 350 μm maps has a size of ∼48″, with a major-axis of 65″.

Finally, we inspected how the algorithm decomposes sources into individual substructures. We tested how blended sources are identified as a single or as a couple of individual objects,

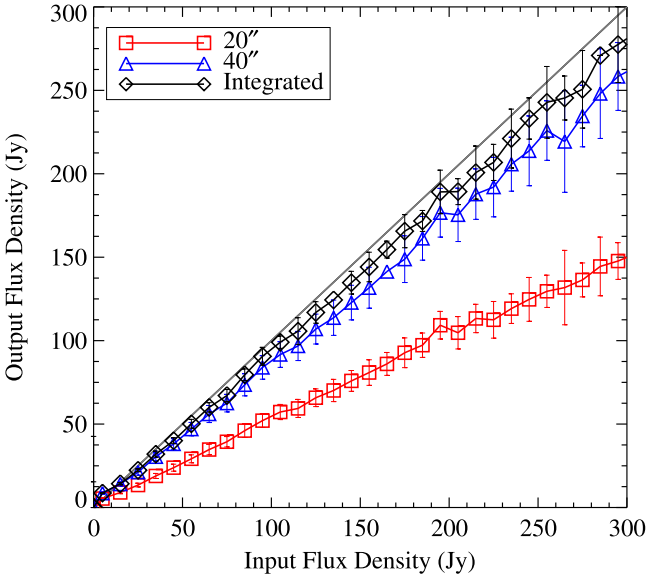

Figure 6. Recovery of source flux density for simulated resolved sources (FHWM $= 2.7\theta_{\rm beam} = 23''$) in SHARC-II maps. Results of the calibrated flux recovery are shown in units of Jy. Small differences are found between the $40''$ aperture and the integrated flux, with an under estimation of the integrated flux of $\sim$10%.

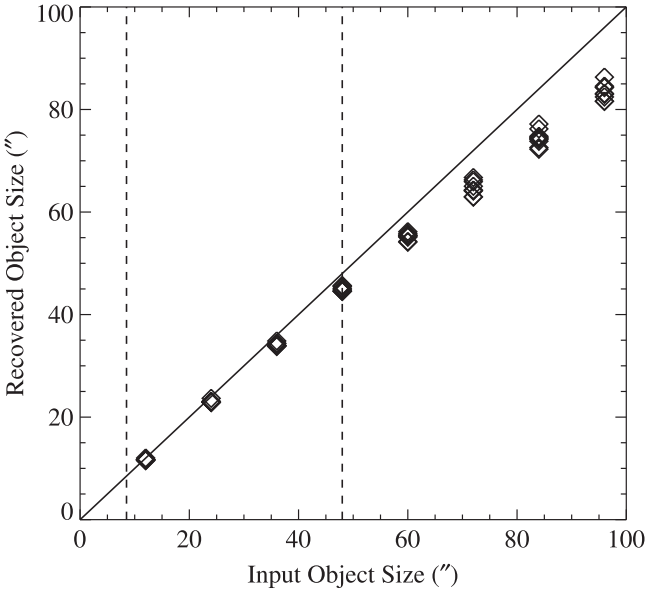

Figure 7. Recovery of source size for simulated observations in SHARC-II maps. The vertical lines at 8.″5 and $48''$ indicate, respectively, the beam size of the images, and the largest size recovered by *Bolocat* for identified objects in our sample of maps. The largest major-axis recovered for identified sources is $65''$.

considering pairs of input objects in the set of test maps. Each source of the pair of input fake sources have sizes between $14''$ and $34''$, and peak flux density of $50\sigma_{\rm rms}$. Figure 8 shows the fraction of blended sources as a function of the separation between pairs of input sources. In general, sources at a distance less than the beam FWHM cannot be recovered individually and they are assigned to the same source in the recovered catalog, and more than 50% of the pairs of input sources are recovered individually at distances larger than $20''$ (2.4 times the beam size). Figure 8 also shows that pairs of input sources with sizes less than $24''$ are better resolved at shorter distance than pairs with larger sizes than that. Pairs of sources are resolved more than 50% at separations of $16''$ for small input sources, and at $25''$ for larger sources.

4.4. Catalog of Sources in the 350 μm Maps

We have recovered from the *Bolocat* extraction 1386 sources in the 350 μm maps. We name our sources in a similar way as described in the BGPS catalog, using the peak position of the source in galactic coordinates: SHARC_G *lll.llll* $\pm$ *bb.bbbb*. An additional digit with respect to the BGPS catalog was required to account for the better resolution and smaller pixel size in the SHARC-II maps. Table 3 presents the properties recovered for the extracted sources. The positions of the recovered sources in the SHARC-II maps are shown in Figure 25 in the Appendix.

Figure 9 shows the distribution of recovered flux for these sources using three methods from our catalog: photometry in $20''$ and $40''$ apertures, and the integrated flux. For the $20''$ aperture, the average and median value of the flux density are 23.15 $\pm$ 1.59 and 8.95 Jy, respectively. For the $40''$ aperture, the average and median values are 45.11 $\pm$ 2.82 and 16.63 Jy, respectively. For the integrated flux density, the average and median values are 59.59 $\pm$ 5.19 and 12.06 Jy, respectively.

Figure 10 shows the deconvolved radii and the aspect ratio distribution. The deconvolved radius distribution extends to $46''$, and the catalog has 257 sources ($\sim$19% of the total) with radii not resolved. These small sources are usually faint, with an average value of their peak S/N of 4.4. The average and median of the radius distribution are 15.″0 and 14.″0, respectively. The aspect ratio is defined as $\sigma_{\rm maj}/\sigma_{\rm min}$, and its average and median values are 1.53 and 1.45, respectively. A similar median aspect ratio is found in the BGPS V2.1 catalog, and this could be a common feature of millimeter and submillimeter sources, or an artifact of the extraction algorithm.

4.5. Correlation with BGPS Sources

We performed a spatial position matching analysis to get a correlation between sources found in the 350 μm maps and the BGPS V2.1 sources contained in them. Therefore, we excluded from this analysis the three maps of outer Galaxy regions outside the coverage area of BGPS. A simple criterion to match sources from catalogs at different resolutions is to take the position of maximum intensity for sources of one catalog and find which sources in the second catalog are one beam distant from that position. For example, Contreras et al. (2013) performed this kind of matching between sources of the ATLASGAL survey (870 μm, 19.″2 FWHM beam size) and BGPS V1.0 sources, considering that sources between these catalogs are associated if their peak positions are less than $40''$ in angular distance, finding around $\sim$3000 likely matches. One of the issues with this approach is that it does not yield a one-to-one association. This has special importance in catalogs based on sources extracted from maps at different resolutions. Even more, Ginsburg et al. (2013) found that for the same 1.1 mm data at $33''$ FWHM beam resolution, re-processed V2.1 maps with better spatial filtering recover in some cases more than the one source that previous V1.0 maps found, and in others V2.1 maps recover a single structure where V1.0 recovered many. Then, sources required more than simple

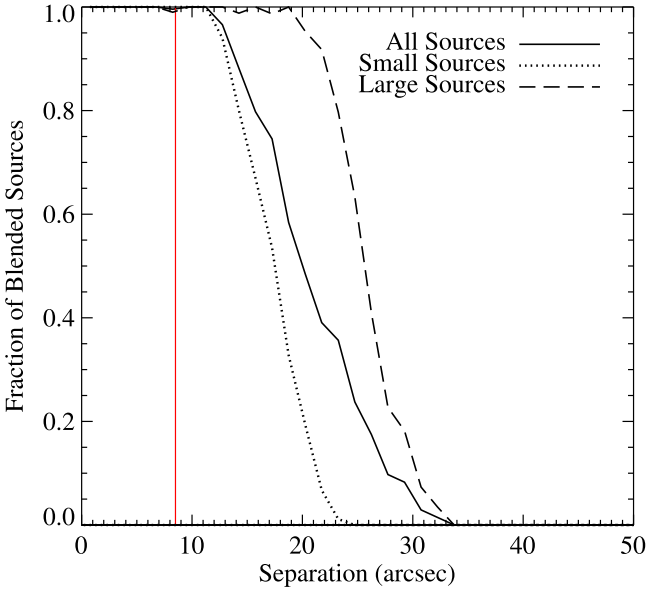

Figure 8. Fraction of blended fake objects as a function of source pair separation (solid line). The vertical red line shows the FWHM beam size of the 350 μm maps. Smaller input sources (15″–24″ in size) are represented by the dotted line, and large input sources (24″–34″ in size) are represented by segmented line.

matching at beam distance to compare different versions of the catalog.

Considering the different beam size of the 350 μm maps (8.″5) and 1.1 mm maps (33″), we expect to resolve extended millimeter sources in some cases into multiple smaller components, and we put the constraint that compact sources identified in the 350 μm maps must be associated with a single 1.1 mm source. For the following analysis, we will consider as a "parental clump" a 1.1 mm source from the BGPS catalog harboring one or more associated matched structures on the 350 μm maps, which we will refer to as "high-resolution sources" or just simply as "substructures."

We made use of one of the sub-products of the *Bolocat* algorithm, the mask produced for each map in the identification of individual significant emission. These *labelmask* maps give information on which particular position in a map contains emission and associates that position with a single source from the catalog produced for that map. Our approach was taking the position of maximum intensity from the 350 μm sources, and if that peak is within the *labelmask* of a BGPS V2.1 source, it is considered associated.

For the sample of 104 SHARC-II maps containing BGPS sources, there are 1374 high-resolution sources. Only 24 (2%) of those sources have their peak position not associated with a BGPS V2.1 source from the *labelmask* maps. The association between 350 μm high resolution sources and 1.1 mm sources suffers from intrinsic, noise driven uncertainty in the peak flux density position and the algorithm uncertainties in the *labelmask* area assigned to a specific source. We improved the matching of sources considering also the *labelmask* maps of the 350 μm emission overlapping both masks and estimating how much of the substructure mask area is associated with the parental source in the BGPS *labelmask* area. Two of the 24 sources have most of their mask area associated with a parental source and therefore are re-considered as matched sources. For the sample 350 μm sources with a match, there are 17 sources with their mask area shared between two parent sources, and for them we made a visual inspection to see the most likely correct parental association. Figure 11 shows a couple of examples for association between 350 μm and 1.1 mm *labelmask* regions.

We obtained a total of 1352 high-resolution sources associated with 349 different parental sources. The results of the previously described spatial matching of 350 μm SHARC-II and 1.1 mm BGPS sources are shown in Figure 12. Half of the parental clumps have only one or two associated high-resolution sources, but toward several of the parental clumps we found a large multiplicity of sources, indicating possible fragmentation. The clumps with the largest multiplicity are BGPSv2_G213.705-12.603 (34 substructures), BGPSv2_G034.256+00.154 (27), BGPSv2_G133.716+01.220 (25), BGPSv2_G000.014-00.017 (23), BGPSv2_G029.916-00.045 (22), BGPSv2_G081.477+00.020 (20), and BGPSv2_G029.958-00.017 (19). There are 22 parental millimeter sources with more than 10 substructures, containing a total of 350 high-resolution sources (26% of the total).

These parental sources show some clear strong compact sources in them, but also some elongated, filamentary structures are present. We explored whether the large number of substructures in parental sources is due to spurious low brightness sources and/or algorithm fragmentation of large sources. We consider the peak signal-to-noise ratio (S/N) identified for each source by *Bolocat* and compare the number of identified sources under different ranges of this ratio. Table 4 presents the number of substructures with amplitude $P_{\rm amp}$ (described in Section 4.2) above $6\sigma_{\rm rms}$, $10\sigma_{\rm rms}$ and $20\sigma_{\rm rms}$ for the 22 BGPS sources with large multiplicity. For these, 66% of 350 μm sources have $P_{\rm amp}$ of $6\sigma_{\rm rms}$, 42% of $10\sigma_{\rm rms}$, and 19% of $20\sigma_{\rm rms}$. Figure 11 shows two examples of the distribution at different peak S/N levels for two of these parental sources. While compact, strong sources have $P_{\rm amp}$ above $10\sigma_{\rm rms}$, detections below this limit recover not only isolated low emission objects but also filament-like features in chains of sources and weak detections produced in the decomposition process of the algorithm. We conclude then that sources with $P_{\rm amp}$ above $10\sigma_{\rm rms}$ ("compact substructure") are more related with possible dense core-like structures in the interior of millimeter clumps, and sources below this limit ("faint substructure") trace a more diffuse medium in addition to weak sources. For the total number of high-resolution sources recovered from the SHARC-II maps, only 437 (∼32%) are considered compact substructures. Column 14 in Table 3 indicates if a source recovered in the 350 μm maps is "compact" or "faint."

4.6. Flux densities of BGPS sources at 350 μm

We determined the flux densities at 350 μm of BGPS V2.1 sources by measuring the flux density in an aperture of 40″ on our sample of SHARC-II maps. To match the 33″ FWHM effective BGPS beam at 1.1 mm, the 350 μm images, (1.″618 per pixel) were convolved with Gaussian kernels (using IRAF task GAUSS) having $\sigma = 13.''5$ (8.33 pixels), i.e., convolving with a Gaussian FWHM $=\sigma\sqrt{8\ln 2} = 31.''8$.

From the total of 619 BGPS V2.1 sources in the 350 μm maps, there are 82 sources that appear in more than one map;

Table 3
Properties of Sources Recovered in the 350 μm Maps

No.	Name	l_{max} (°)	b_{max} (°)	l (°)	b (°)	σ_{maj} (″)	σ_{min} (″)	P.A. (°)	Θ_R (″)	S_{20} (Jy)	S_{40} (Jy)	S (Jy)	Type
(1)	(2)	(3)	(4)	(5)	(6)	(7)	(8)	(9)	(10)	(11)	(12)	(13)	(14)
1	SHARC_G000.0002-00.0200	0.0002	–0.0200	359.9995	–0.0175	8	6	36	15	42.91 ± 4.51	118.56 ± 11.11	100.41 ± 6.94	F
2	SHARC_G000.0006-00.0246	0.0006	–0.0246	359.9994	–0.0253	7	6	64	13	55.84 ± 5.86	122.38 ± 11.47	96.41 ± 6.66	C
3	SHARC_G000.0008-00.0304	0.0008	–0.0304	0.0002	–0.0305	5	4	102	7	26.85 ± 2.82	55.23 ± 5.18	26.29 ± 1.82	F
4	SHARC_G000.0013-00.0784	0.0013	–0.0784	0.0008	–0.0780	5	4	142	7	13.62 ± 1.43	23.03 ± 2.17	12.71 ± 0.89	F
5	SHARC_G000.0065-00.0557	0.0065	–0.0557	0.0058	–0.0575	13	8	153	22	49.25 ± 5.17	104.71 ± 9.81	146.57 ± 10.13	C
6	SHARC_G000.0067-00.0146	0.0067	–0.0146	0.0052	–0.0139	6	5	104	9	30.57 ± 3.21	89.52 ± 8.39	37.29 ± 2.58	F
7	SHARC_G000.0075-00.0199	0.0075	–0.0199	0.0058	–0.0208	11	6	67	17	68.11 ± 7.15	162.68 ± 15.24	163.46 ± 11.30	C
8	SHARC_G000.0089+00.0034	0.0089	0.0034	0.0092	0.0035	5	3	17	…	7.53 ± 0.80	13.34 ± 1.26	5.00 ± 0.35	F
9	SHARC_G000.0120-00.0201	0.0120	–0.0201	0.0129	–0.0182	12	8	47	21	80.66 ± 8.47	188.93 ± 17.70	237.90 ± 16.44	C
10	SHARC_G000.0121-00.0513	0.0121	–0.0513	0.0113	–0.0511	9	7	34	17	60.03 ± 6.30	121.66 ± 11.40	122.43 ± 8.46	C
11	SHARC_G000.0130+00.0064	0.0130	0.0064	0.0127	0.0065	9	4	164	10	15.16 ± 1.60	34.25 ± 3.21	21.75 ± 1.51	F
12	SHARC_G000.0135-00.0217	0.0135	–0.0217	0.0156	–0.0233	7	5	165	10	78.04 ± 8.19	161.42 ± 15.12	102.54 ± 7.09	C
13	SHARC_G000.0142+00.0364	0.0142	0.0364	0.0148	0.0359	10	8	111	19	26.86 ± 2.82	48.54 ± 4.55	55.72 ± 3.86	F
14	SHARC_G000.0145+00.0127	0.0145	0.0127	0.0150	0.0125	3	3	169	…	5.00 ± 0.54	7.71 ± 0.74	3.05 ± 0.22	F
15	SHARC_G000.0188+00.0040	0.0188	0.0040	0.0186	0.0072	7	5	20	11	26.13 ± 2.75	59.59 ± 5.58	39.78 ± 2.75	F
16	SHARC_G000.0195-00.0067	0.0195	–0.0067	0.0184	–0.0077	12	6	62	19	32.01 ± 3.36	56.13 ± 5.26	63.15 ± 4.37	F
17	SHARC_G000.0196-00.0501	0.0196	–0.0501	0.0199	–0.0511	12	10	30	24	73.00 ± 7.66	143.62 ± 13.46	208.13 ± 14.38	C
18	SHARC_G000.0197+00.0017	0.0197	0.0017	0.0197	0.0016	6	5	165	10	27.63 ± 2.90	58.82 ± 5.51	34.29 ± 2.37	F
19	SHARC_G000.0238+00.0359	0.0238	0.0359	0.0237	0.0357	11	6	78	16	15.41 ± 1.62	33.58 ± 3.15	33.12 ± 2.30	F
20	SHARC_G000.0247+00.0032	0.0247	0.0032	0.0252	0.0024	7	5	166	11	19.90 ± 2.09	39.84 ± 3.74	26.18 ± 1.81	F
21	SHARC_G000.0279-00.0533	0.0279	–0.0533	0.0279	–0.0538	7	6	14	13	29.31 ± 3.08	79.58 ± 7.46	55.47 ± 3.84	F
22	SHARC_G000.0281-00.0576	0.0281	–0.0576	0.0278	–0.0587	8	4	87	10	23.22 ± 2.44	55.01 ± 5.16	32.71 ± 2.26	F
23	SHARC_G000.0308+00.0211	0.0308	0.0211	0.0303	0.0218	11	7	18	18	35.87 ± 3.77	65.86 ± 6.17	71.75 ± 4.96	F
24	SHARC_G000.0315-00.0512	0.0315	–0.0512	0.0304	–0.0507	5	4	35	7	26.45 ± 2.78	65.31 ± 6.12	26.94 ± 1.86	F
25	SHARC_G000.0331+00.0054	0.0331	0.0054	0.0337	0.0061	8	4	90	8	15.37 ± 1.62	15.11 ± 1.43	16.67 ± 1.16	F

Notes. (1) Running source number. (2) Name derived from Galactic coordinates of the maximum intensity in the object. (3), (4) Galactic coordinates of maximum intensity in the catalog object. (5), (6) Galactic coordinates of emission centroid. (7)–(9) Major and minor axis 1/e widths and position angle of source. (10) Deconvolved angular size of source. (11), (12) Flux densities derived for 20 and 40 apertures. (13) Integrated flux density in the object. (14) Type of substructure: "C"—compact or "F"—faint, as defined in Section 4.5.

(This table is available in its entirety in machine-readable form.)

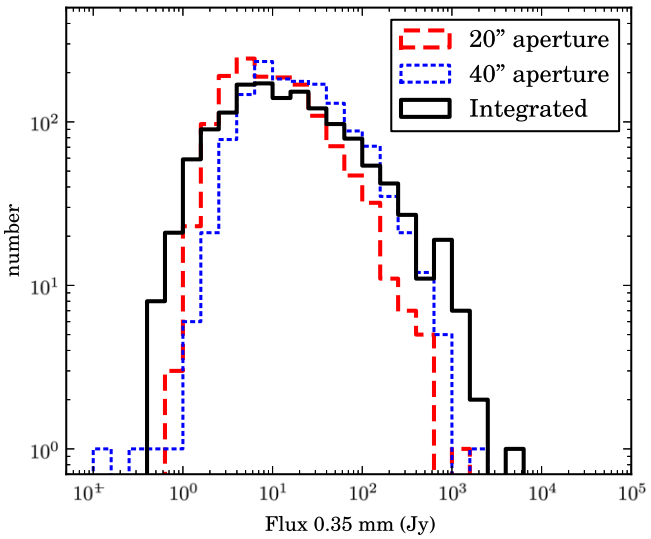

Figure 9. Flux distribution for objects identified in the 107 SHARC-II maps. Three methods of flux recovery are represented in the image: aperture photometry at 20″ (red long dashed line) and 40″ (blue short dashed line) in diameter toward the peak, and integrated emission of the source (solid black line).

we preferred the flux determination from the maps where those sources suffer fewer sampling artifacts, such as high noise due to map edge proximity, or negative bowls around the source. In case there are not evident problems in the source flux estimation, we just considered the averaged result of the flux density. In addition, there are 45 BGPS sources with negative integrated fluxes on the 350 μm maps due to their proximity to noisy edges or negative bowls surrounding areas of strong emission, and therefore these sources are not considered as reliable measurements.

Results of the estimated values of 350 μm continuum emission from BGPS sources are presented in Table 5. Column 1 gives the name of the source in the V2.1 catalog. Column 2 gives the flux density integrated in an aperture of 40″ centered on the peak position of the 1.1 mm source. The values of the flux density are corrected by the factor 1.46 suggested by Aguirre et al. (2011) for the 40″ aperture flux obtained in BGPS catalog. Column 3 gives the integrated flux density for aperture photometry in the same previous position, but this time in the 350 μm convolved maps.

4.7. Comparison between SHARC-II and Herschel Images

From Molinari et al. (2010), we used the Hi-GAL 2° × 2° images at 350 μm obtained during the science demonstration phase centered toward $l = 30°$, $b = 0°$ and compared the results of flux recovery between the *Herschel*/SPIRE image and the 10 SHARC-II maps contained in that area. The *Herschel* image has an FWHM beam resolution of 24.″9, and details in the reduction process are found in Traficante et al. (2011). Figure 26 in the Appendix shows 1.1 mm BGPS images, and their corresponding Hi-GAL images at 350 μm toward $l = 30°$, $b = 0°$, for regions mapped with SHARC-II. While the 1.1 mm images in this figure show the position of the sources from the BGPS V2.1 catalog, the 350 μm images show in blue (<10 σ) or red (>10 σ) the objects identified in our high-resolution source catalog. There are 213 of these substructures found, with only one left out of the following analysis due to noisy edge effects.

First, we compared the flux obtained on the sources recovered directly by *Bolocat* in this set of SHARC-II images, with emission measured in the *Herschel* map. Upper panel of Figure 13 shows the ratio between the density flux at 40″ aperture $F_{\rm SHARC}$ and the recovered flux at the same aperture, centered on the peak position of the high-resolution sources, obtained from the *Herschel* image, $F_{Herschel}$. For faint substructures, the flux ratio is in general below 0.3, with a cut around $F_{Herschel} \sim 100$ Jy, which suggests that the *Herschel* image is recovering additional flux from diffuse, large scale emission that SHARC-II maps do not recover.

Uniform background emission ranging between 2700–3300 MJy sr^{-1} in the *Herschel* image would give a flux density into a 40″ aperture of 80–100 Jy. Figure 14 shows one of the SHARC-II maps toward $l = 30°$, L029.95-0.05, and the *Herschel* emission in the same region. This figure also presents the SHARC-II map convolved to a resolution of 24.9″, to match the beam size of Hi-GAL data at the same wavelength. The emission level at 17σ in the *Herschel* data corresponds to ∼2790 MJy sr^{-1}, and the morphology of emission recovered above that contour level in the *Herschel* map is similar to the structures detected above 3σ level in the SHARC-II images. A "background emission" level for the *Herschel* maps would lie at about 2460 MJy sr^{-1}, corresponding to the 15σ level (white contour in Figure 14), and a 40″ aperture integrated flux density of

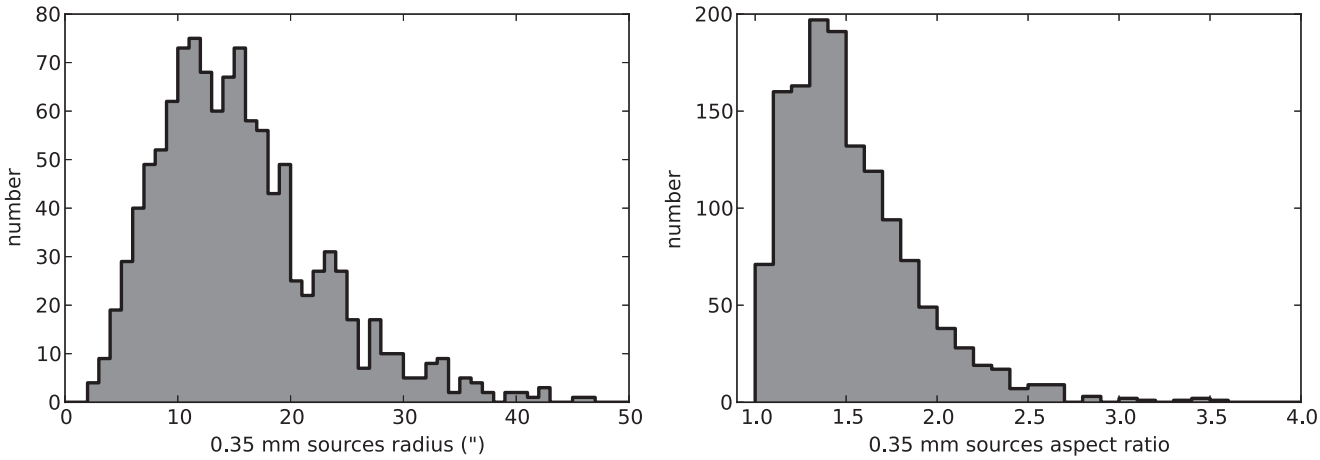

Figure 10. Distribution of the deconvolved radii and aspect ratio of sources in the SHARC-II maps. The average and median values of the radius distribution are 15″ and 14″, respectively. The average and median values of the aspect ratios are, respectively, 1.53 and 1.45.

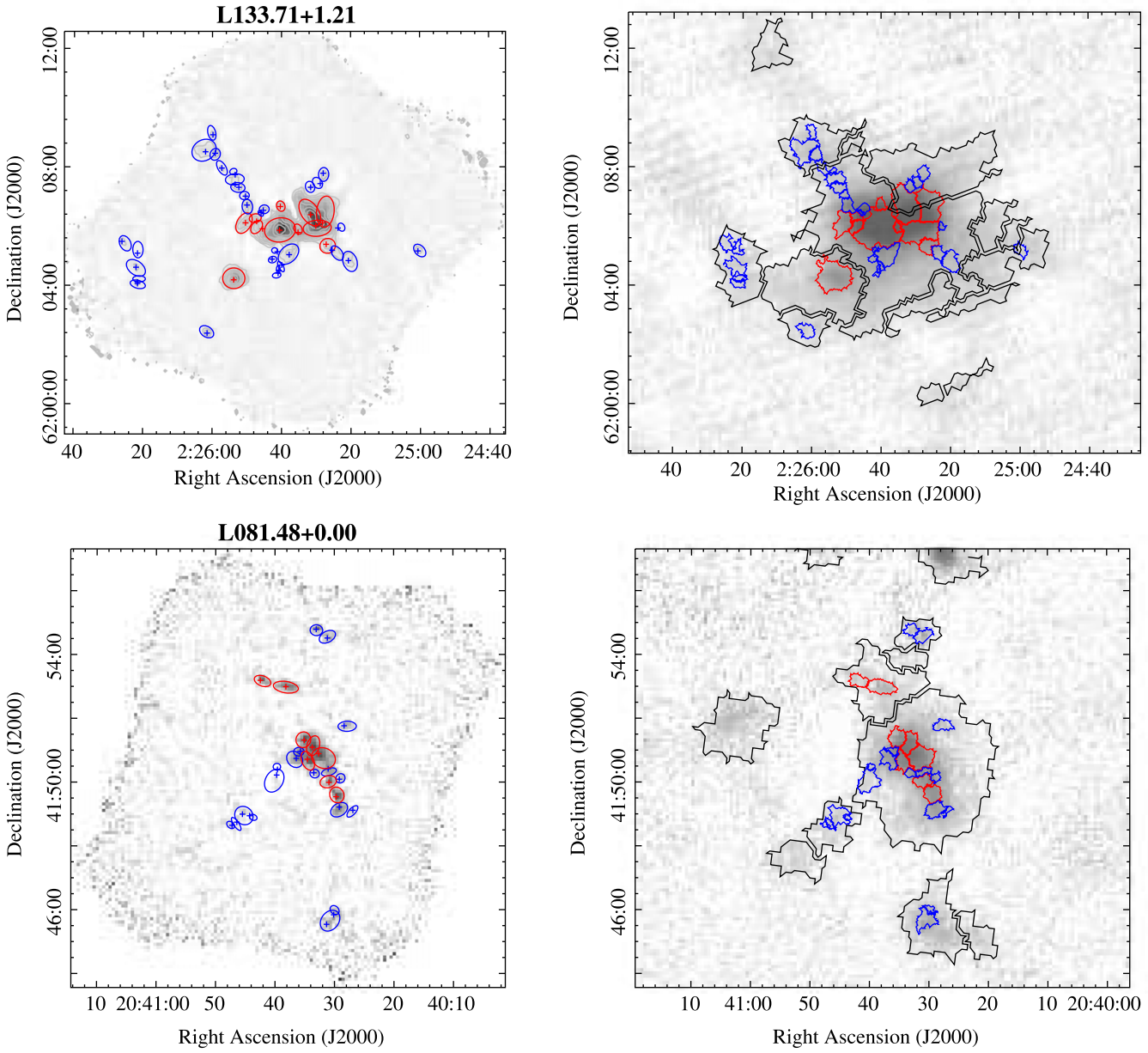

Figure 11. Upper left: results of Bolocat on the 350 μm map of L133.71+1.21, corresponding to the W3 Main region. The different colors indicate the peak signal-to-noise of each source (above 10σ in red, below that limit in blue). Sources in red are associated with compact and dense core-type structures, the blue sources are related to low emission, field material or possible filamentary structure. Upper right: gray color scale of the 1.1 mm toward the same region. Black regions show the result of *Bolocat* on the 1.1 mm map, and blue and red regions the results of *Bolocat* on the 350 μm map. The central V2.1 source mask shows large number of substructures (both strong and faint). Lower panels are similar to the upper panels for L081.48+0.00, in the Cygnus X region. The comparison of source masks reveal a large population of BGPS V2.1 sources located inside the 350 μm maps, but not associated with any source at high-resolution. Details on the correlation between 350 μm sources and their parental BGPS clump are described in Section 4.5.

~73 Jy. The beam-matched SHARC-II image shows that the 1σ emission level has a good resemblance to that background emission level.

Inspecting Figure 26, most of the faint substructures do not look like well-defined entities at a 10σ contour, but instead they seem to be immersed in background extended emission. For the compact substructures recovered in the SHARC-II maps, the average and median values for the flux ratio are 0.56 $\pm$ 0.03 and 0.53, respectively. For those high-emission compact sources with peak S/N above 50, represented by green points in Figure 13, flux recovery in the SHARC-II maps and the *Herschel* map are nearly the same (average flux ratio of 1.00 $\pm$ 0.11).

We performed a similar analysis for the 102 BGPS sources found in this region. We first convolved the 350 μm *Herschel* image to match the 33″ resolution of Bolocam and later compare the 40″ aperture flux emission obtained toward the peak position of BGPS sources. Results are shown in bottom panel of Figure 13. Errors in the flux ratio consider conservative uncertainties of 20% in the flux from the *Herschel* image and 30% in fluxes from SHARC-II data. Sources without any substructure associated have low mm emission and flux ratio $F_{\rm SHARC}/F_{Herschel}$ on average lower than 0.1. For those 1.1 mm parental clumps associated with compact substructures (shown in red in the figure), the average and median values of the flux ratio are 0.76 $\pm$ 0.08 and 0.69, respectively.

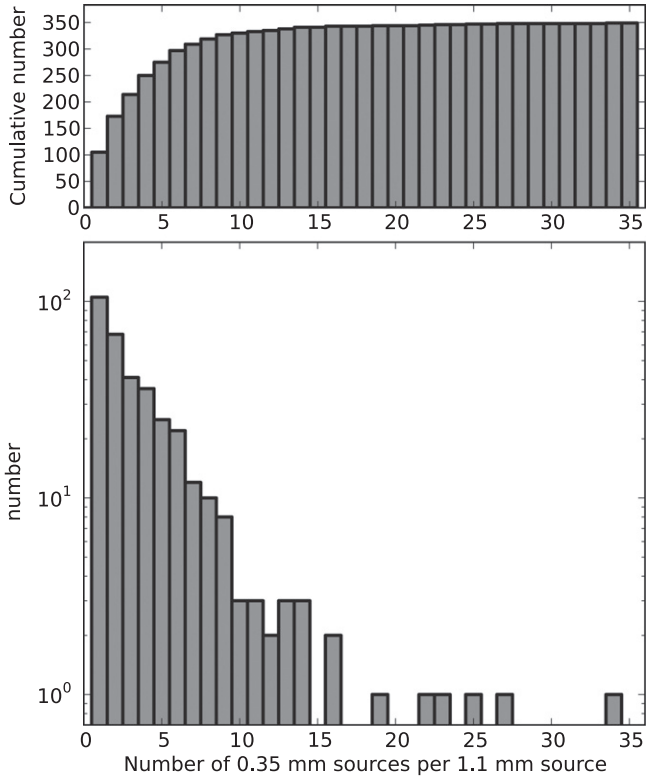

Figure 12. Distribution of 350 μm sources per 1.1 mm source from BGPS. The top panel shows the cumulative number. Half of the 1.1 mm parental clumps are associated with one or two substructures identified at high-resolution.

Table 4
Sources from the BGPS Catalog with a Large Number of High-resolution Associated Substructures

BGPS V2.1 name	Peak Emission of 350 μm Substructures			
	Total[a]	>6$\sigma_{\rm rms}$	>10$\sigma_{\rm rms}$	>20$\sigma_{\rm rms}$
BGPSv2_G213.705-12.603	34	24	15	12
BGPSv2_G034.256+00.154	27	18	15	8
BGPSv2_G133.716+01.220	25	15	9	4
BGPSv2_G000.014-00.017	23	9	5	1
BGPSv2_G029.916-00.045	22	18	8	3
BGPSv2_G029.958-00.017	19	13	6	4
BGPSv2_G359.867-00.083	16	12	8	4
BGPSv2_G081.477+00.020	16	11	6	0
BGPSv2_G359.982-00.069	14	12	7	1
BGPSv2_G359.946-00.045	14	5	1	0
BGPSv2_G030.751-00.051	14	8	7	5
BGPSv2_G081.753+00.593	13	9	7	5
BGPSv2_G076.359-00.600	13	11	7	1
BGPSv2_G030.786-00.025	13	12	11	3
BGPSv2_G203.223+02.076	12	8	1	0
BGPSv2_G192.598-00.049	12	7	5	1
BGPSv2_G203.320+02.058	11	7	6	4
BGPSv2_G023.437-00.183	11	5	2	1
BGPSv2_G023.273-00.211	11	7	1	0
BGPSv2_G081.721+00.573	10	9	8	7
BGPSv2_G030.690-00.043	10	4	3	0
BGPSv2_G024.493-00.039	10	7	6	3

[a] Total number of associated substructures (compact and faint) found on SHARC-II maps per each BGPS parental clump. See Section 4.5 for details.

We emphasize that the differences arise from the better angular resolution of SHARC-II compared to *Herschel*/SPIRE data and not properly to the background subtraction; SHARC-II images are better able to disentangle the very dense and inner parts of clumps from the surrounding diffuse emission.

5. ANALYSIS

5.1. Temperature Determination

The data at 350 μm and 1.1 mm can be used to define a color temperature. We will refer to this quantity through this analysis as the "dust temperature," although variations in temperature across and along the line of sight make this color temperature only a rough guide to the actual dust temperatures.

The observed intensity of continuum emission is given by $S_\nu = \Omega_{\rm beam}[1 - e^{-\tau_{\nu d}}]B_\nu(T_d)$, where $\Omega_{\rm beam}$ is the beam solid angle (33″ beam) for both the 1.1 mm data and the convolved, beam matched, 350 μm observations, $\tau_{\nu d}$ is the optical depth of the emitting dust at each frequency and $B_\nu(T_d)$ is the Planck function at the dust temperature T_d. The optical depth in the submm to mm regime is considered proportional to ν^β. In the optically thin limit, the temperature can be estimated according to:

$$R = \frac{S_{350\,\mu\rm m}}{S_{1.1\,\rm mm}} = \frac{\nu_{350\mu\rm m}^{3+\beta}\left[\exp\left(h\nu_{1.1\,\rm mm}/kT_d\right) - 1\right]}{\nu_{1.1\,\rm mm}^{3+\beta}\left[\exp\left(h\nu_{350\,\mu\rm m}/kT_d\right) - 1\right]}. \quad (1)$$

$S_{350\,\mu\rm m}$ and $S_{1.1\,\rm mm}$ are the integrated flux densities obtained in 40″ apertures in the convolved SHARC-II maps and in the BGPS maps, respectively. The distribution of the ratio $S_{350\,\mu\rm m}/S_{1.1\,\rm mm}$ for the 574 V2.1 sources with reliable flux values is shown in Figure 15. The ratio distribution has a maximum of 181.0, with a median value of 19.7.

Equation (1) cannot be solved analytically for T_d. The adjustment of the pair of parameters T_d and β has been a recurrent issue in the study of the interstellar medium and star formation. Frequently, a value of $\beta \sim 2$ in the millimeter to submillimeter regime is assumed, referring to studies of dust grains composed by graphite and silicate (Draine & Lee 1984), but models with variations of ice mantles due to coagulation give lower values (e.g., Ossenkopf & Henning 1994 estimated $\beta = 1.8$ for their OH5 model). Values near $\beta \sim 1$ may be appropriate for circumstellar disks (e.g., Beckwith & Sargent 1991). Shirley et al. (2005) summarize different opacity models in the submillimeter–millimeter regime for low-mass pre-protostellar cores, with values of β between 1.3 and 2.3. For the present analysis, we obtained dust temperatures considering three different values of β: 1.0, 1.7, and 2.0. Nevertheless, considering that most BGPS sources properties are related to dust clumps of dense material, $\beta = 1.7$ should be the closest model of the true nature of these structures. Figure 16 shows the fitted values for temperatures as a function of the ratio $S_{350\,\mu\rm m}/S_{1.1\,\rm mm}$ for the three models previously described. For $\beta = 1.7$, uncertainties in the determination of temperatures are shown in the figure, considering an error of the flux ratio of 10%.

The large uncertainty for high temperatures is unavoidable with these data. At high temperatures (>50 K, see below), both 1.1 mm and 350 μm flux densities approach the Rayleigh–Jeans limit, and therefore the ratio becomes nearly constant,

Table 5
BGPS V2.1 Sources Fluxes and Fitted Dust Temperature

BGPS Source	1.1 mm Flux 40″ (Jy)	Convolved 350 μm[a] Flux 40″ (Jy)	Temperature $\beta = 1.0$ (K)	Temperature $\beta = 1.7$ (K)	Temperature $\beta = 2.0$ (K)
BGPSv2_G024.743+00.179	0.51 ± 0.11	17.82 ± 0.64	>1000.0 $^{>1000.0}_{103.1}$	23.5 $^{31.1}_{18.3}$	16.7 $^{19.9}_{14.1}$
BGPSv2_G024.745+00.161	0.60 ± 0.12	18.42 ± 0.66	351.7 $^{>1000.0}_{58.2}$	20.2 $^{24.8}_{16.6}$	15.1 $^{17.3}_{13.1}$
BGPSv2_G024.757+00.091	1.36 ± 0.12	61.75 ± 2.19	>1000.0 $^{>1000.0}_{>1000.0}$	34.9 $^{42.9}_{29.2}$	21.2 $^{23.6}_{19.1}$
BGPSv2_G024.759+00.065	0.43 ± 0.09	8.47 ± 0.38	33.3 $^{52.7}_{23.4}$	14.2 $^{16.2}_{12.3}$	11.6 $^{12.9}_{10.4}$
BGPSv2_G024.760+00.163	0.34 ± 0.13	4.80 ± 0.18	20.8 $^{31.9}_{14.2}$	11.7 $^{14.0}_{9.5}$	10.0 $^{11.5}_{8.4}$
BGPSv2_G024.773+00.125	0.22 ± 0.09	1.67 ± 0.07	12.9 $^{16.2}_{9.9}$	8.9 $^{10.3}_{7.5}$	8.0 $^{8.9}_{6.8}$
BGPSv2_G024.791+00.083	10.07 ± 0.64	556.65 ± 19.73	>1000.0 $^{>1000.0}_{>1000.0}$	58.6 $^{78.9}_{46.3}$	27.1 $^{30.2}_{24.4}$
BGPSv2_G024.795+00.101	3.14 ± 0.22	142.57 ± 4.87	>1000.0 $^{>1000.0}_{>1000.0}$	34.8 $^{41.0}_{30.1}$	21.2 $^{23.0}_{19.5}$
BGPSv2_G024.807+00.039	0.32 ± 0.09	5.84 ± 0.23	29.1 $^{49.6}_{19.4}$	13.5 $^{16.0}_{11.3}$	11.2 $^{12.7}_{9.7}$
BGPSv2_G024.815+00.189	0.10 ± 0.09	-0.75 ± 0.05	… $^{\ldots}_{\ldots}$	… $^{\ldots}_{\ldots}$	… $^{\ldots}_{\ldots}$
BGPSv2_G024.817+00.129	0.48 ± 0.09	6.69 ± 0.27	20.7 $^{25.5}_{17.0}$	11.6 $^{12.8}_{10.5}$	9.9 $^{10.7}_{9.1}$
BGPSv2_G024.824+00.181	0.17 ± 0.09	1.89 ± 0.07	16.5 $^{25.0}_{10.7}$	10.3 $^{12.7}_{7.9}$	9.0 $^{10.7}_{7.2}$
BGPSv2_G024.850+00.085	0.90 ± 0.11	36.60 ± 1.32	>1000.0 $^{>1000.0}_{>1000.0}$	28.9 $^{35.9}_{23.7}$	19.0 $^{21.5}_{16.8}$
BGPSv2_G024.863+00.145	0.16 ± 0.09	1.08 ± 0.04	12.2 $^{16.4}_{8.4}$	8.6 $^{10.3}_{6.7}$	7.7 $^{9.0}_{6.1}$
BGPSv2_G025.329-00.196	0.56 ± 0.12	3.95 ± 0.16	12.4 $^{13.9}_{10.9}$	8.7 $^{9.4}_{8.0}$	7.8 $^{8.3}_{7.2}$
BGPSv2_G025.339-00.170	0.19 ± 0.12	0.76 ± 0.04	9.5 $^{11.7}_{7.0}$	7.3 $^{8.4}_{5.8}$	6.6 $^{7.5}_{5.4}$
BGPSv2_G025.355-00.156	0.19 ± 0.13	1.49 ± 0.08	13.2 $^{19.5}_{8.0}$	9.1 $^{11.3}_{6.4}$	8.1 $^{9.7}_{5.9}$
BGPSv2_G025.355-00.190	1.46 ± 0.15	40.94 ± 1.53	116.1 $^{738.0}_{61.5}$	18.6 $^{20.6}_{16.8}$	14.2 $^{15.3}_{13.2}$
BGPSv2_G025.382-00.182	3.23 ± 0.24	115.44 ± 4.01	>1000.0 $^{>1000.0}_{>1000.0}$	24.0 $^{26.7}_{21.8}$	17.0 $^{18.1}_{15.9}$
BGPSv2_G025.399-00.140	4.56 ± 0.31	152.14 ± 5.34	>1000.0 $^{>1000.0}_{405.7}$	22.1 $^{24.1}_{20.3}$	16.1 $^{17.0}_{15.1}$
BGPSv2_G025.405-00.256	0.31 ± 0.15	3.14 ± 0.11	15.8 $^{23.1}_{10.6}$	10.1 $^{12.3}_{7.9}$	8.8 $^{10.4}_{7.1}$
BGPSv2_G025.413-00.176	0.65 ± 0.12	17.80 ± 0.64	98.2 $^{>1000.0}_{43.3}$	18.2 $^{21.6}_{15.4}$	14.0 $^{15.8}_{12.4}$
BGPSv2_G025.455-00.210	1.64 ± 0.17	75.41 ± 2.61	>1000.0 $^{>1000.0}_{>1000.0}$	35.9 $^{46.0}_{29.1}$	21.5 $^{24.4}_{19.1}$
BGPSv2_G025.467-00.126	0.12 ± 0.12	0.33 ± 0.06	8.4 $^{11.2}_{\ldots}$	6.7 $^{8.2}_{\ldots}$	6.1 $^{7.4}_{\ldots}$
BGPSv2_G025.477-00.136	0.10 ± 0.12	1.73 ± 0.06	27.0 $^{>1000.0}_{\ldots}$	13.1 $^{25.9}_{\ldots}$	10.9 $^{17.8}_{\ldots}$

[a] Fluxes were obtained from SHARC-II maps convolved to match a 33″ beam size (see Section 4.6).

(This table is available in its entirety in machine-readable form.)

significantly increasing the uncertainty in the determination of T_d.

The computed temperatures using three different values of β are presented in Table 5. Columns 4 and 5 give the source color temperature determined from Equation (1), using a emissivity index $\beta = 1.0$, and the upper and lower limit for that temperature. Values of temperatures and upper and lower limits for a spectral index of $\beta = 1.7$ and $\beta = 2.0$ are given in Columns 6–7 and 8–9, respectively.

From Equation (1), sources with flux ratio $S_{350\,\mu m}/S_{1.1\,mm}$ below 70.2 have temperatures lower than 1000 K for $\beta = 1.7$. Only 32 V2.1 sources (∼6% of sample) have estimated temperatures above 1000 K, most of them (24) found toward the Galactic center region. In only one source, the large flux ratio is the consequence of low emission at 1.1 mm and comparable noise level, and almost half of the rest have $S_{1.1\,mm} > 1$ Jy, which included well-known regions such as G034.256+00.154, G029.958-00.017, G030.702-00.067, and the "Brick" IRDC (Longmore et al. 2012). These very high temperatures reflect flux density ratios near those expected in the Rayleigh–Jeans limit, and the temperatures are not constrained by our data. A centrally heated region will produce strong 350 μm emission; using a ratio with the 1.1 mm emission, which traces a larger region of cold dust, can produce an artificially high color temperature.

At a limiting temperature of 50 K, the corresponding flux ratio is 52.7 for $\beta = 1.7$, and a variation of 10% of this ratio will give an increase of 40% in the estimated temperature. Therefore, to avoid large uncertainties we consider as a "good fit" a determined temperature less or equal than 50 K, and a similar limiting temperature value is found for $\beta = 1.0$ and $\beta = 2.0$. There are 512 sources in our sample below this limit for $\beta = 1.7$, and 30 sources with temperatures between 50 and 290 K with quite large uncertainties.

Figure 17 shows the temperature distribution for the 512 sources, assuming $\beta = 1.7$, with good fits for temperature. The median value is 13.3 K, with an average of 16.3 ± 0.4 K. The difference between the median and the average is explained by the positive skewness of the distribution. The figure also shows the distribution of sources with different models for the spectral index. Considering a value of $\beta = 1.0$, the sample of V2.1 sources tends to have larger values of temperature and then the number of these sources with $T_d \leqslant 50$ K is 322, with a median value of 17.3 K and an average of 19.6 ± 0.5 K. For $\beta = 2.0$, the distribution of fitted temperatures has lower values, with 543 sources below 50 K, and with median and average temperatures of 11.2 K and 13.3 ± 0.3 K, respectively.

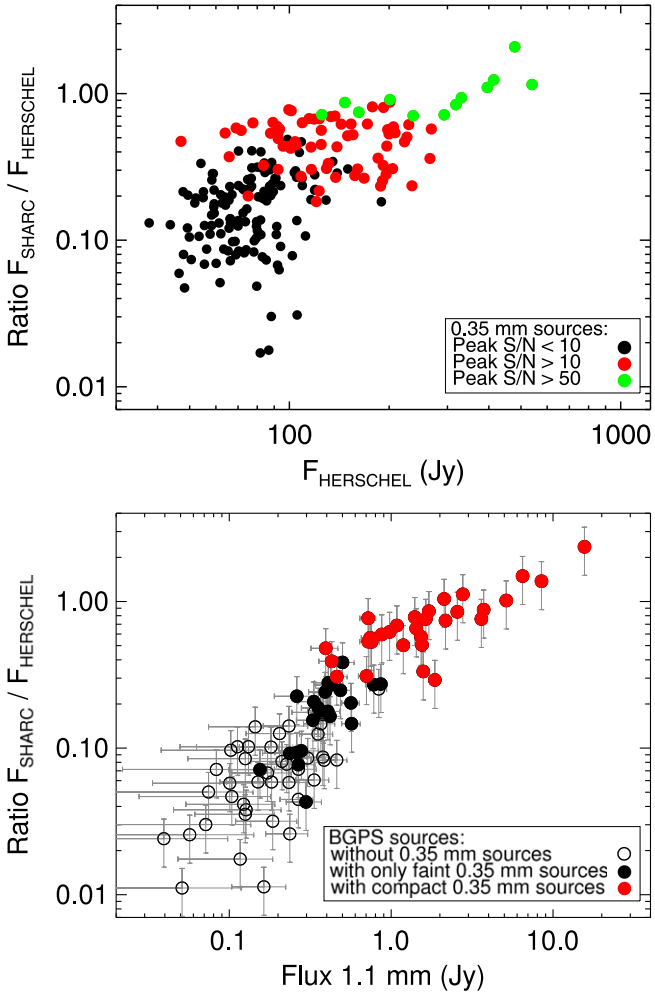

Figure 13. Upper: comparison between integrated flux in 40″ apertures obtained at 350 μm on SHARC-II and *Herschel* images toward $l = 30°$. The points represent the 213 high-resolution sources recovered by *Bolocat* in SHARC-II maps, and the colors show different limits of peak signal-to-noise on those sources. Bottom: comparison between integrated flux in 40″ apertures for 350 μm images from SHARC-II and *Herschel* image on a sample of 102 BGPS sources located toward $l = 30°$. Both SHARC-II and *Herschel* were convolved to match the resolution of the Bolocam maps (33″). Unfilled circles represent BGPS sources with no associated source detected at 350 μm, and filled circles show the 1.1 mm parental clumps with only faint objects (black) and with compact substructures (red). The error bars in the flux ratio considered 20% uncertainties in $F_{Herschel}$, and 30% in $F_{\rm SHARC}$.

Figure 18 plots temperature versus flux density at 1.1 mm for a fixed value $\beta = 1.7$. For faint mm sources, uncertainties in the flux dominate the uncertainties in the temperature. In contrast, temperatures above 30–40 K are uncertain because of the weak constraints as the Rayleigh–Jeans limit is approached. The figure also shows the presence of 8 sources with high flux density (>4 Jy at 1 mm) and low estimated temperatures (<20 K). These are BGPSv2_G359.946-00.045 on the Galactic center region, BGPSv2_G075.834+00.400 and BGPSv2_G076.384-00.622 on Cygnus-X, BGPSv2_G133.716+01.220 on W3 main, BGPSv2_G031.411+00.307, and the sources BGPSv2_G206.557-16.361 and BGPSv2_G206.534-16.356 on NGC 2024, toward the Orion B South molecular cloud. In the case of BGPSv2_G133.716+01.220, corresponding to W3 East, Rivera-Ingraham et al. (2013) recovered a higher temperature (~30 K for $\beta = 2.0$) for this source using *Herschel* data from the HOBYS program (Motte et al. 2010), a difference that is explained in part for the underestimation of the flux at 350 μm due to a shift on the peak of the BGPS source (and therefore the integration aperture) and the peak of the source on the SHARC-II map. In fact, there is a better agreement among the sources W3 West (BGPSv2_G133.698+01.216; $T_d = 28$K, $\beta = 2.0$) and W3 SE (BGPSv2_G133.747+01.198; $T_d = 25$ K, $\beta = 2.0$) and the values estimated by Rivera-Ingraham et al. for these clumps (~25 K and ~21 K, respectively).

In the case of the clump associated to the G31.41+0.31 hot core (Cesaroni et al. 1994), an isothermal temperature of $T = 29$ K was estimated for this source by Mueller et al. (2002) from continuum data modeling, which could indicate that the low temperature is the result of unreliability on the measurement of derived fluxes.

For the two clumps on the Orion B cloud, Johnstone et al. (2006) considered for both sources a temperature of 50 K, though they were unable to obtain color temperatures for them from SCUBA 450 and 850 μm continuum data due to high flux ratios, inconsistent with modified blackbody emission.

There are other 22 sources with $S_{1.1\,\rm mm} > 1$ Jy and $T_d < 15$ K. These sources could be dense, prestellar clumps, but further observations and analysis, particularly in molecular line observations of high-density tracers, are necessary to test their nature.

5.2. Comparison of Temperatures with Other Surveys

We found in general a good agreement between our determination of temperatures and estimations of temperature from other surveys of high-mass star-forming regions. In this section, we describe details of these comparisons.

Faúndez et al. (2004) performed an analysis of physical properties of 146 continuum emission structures detected at 1.2 mm with SIMBA toward *IRAS* sources associated with CS(2–1) detections. The temperature and spectral index of these sources were obtained from SED fitting using additional *IRAS* four band fluxes, obtaining values for β ranging between 1.5 and 2.5, with an average temperature for their sample of ~32 K. Temperatures found for their millimeter structures are larger than ours because their sample was biased toward *IRAS* sources that are intrinsically warm. Their sample has strong emission at 1.2 mm, with all their sources (except one) above 1 Jy and with an average flux density of 16.3 ± 3.2 Jy. Considering the emission at 1.1 mm from our sources that are, within uncertainties and corrections, comparable with their sample, the average temperature for the 124 V2.1 sources with 40″ aperture flux at 1.1 mm above 1 Jy is ~38 K for $\beta = 1.7$. Similarly, Mueller et al. (2002) modeled SEDs of a group of 51 massive star-forming clumps, originally selected by having water masers, and found that a temperature of 29 ± 9 K best characterized the sources. Cross-matching their sample with BGPS sources inside SHARC-II maps, considering one beam (33″) in distance associations between samples, we found 13 BGPS clumps with good determination of dust temperature associated with the sources in Mueller et al. (2002). These sources have average and median values for their 40″ aperture integrated flux of 8.5 and 7 Jy, respectively, with only one source with integrated flux below 1 Jy. One of these sources corresponds to BGPSv2_G031.411+00.307, for which its fitted dust temperature is considered underestimated (see Section 5.1). Excluding this source, the fitted

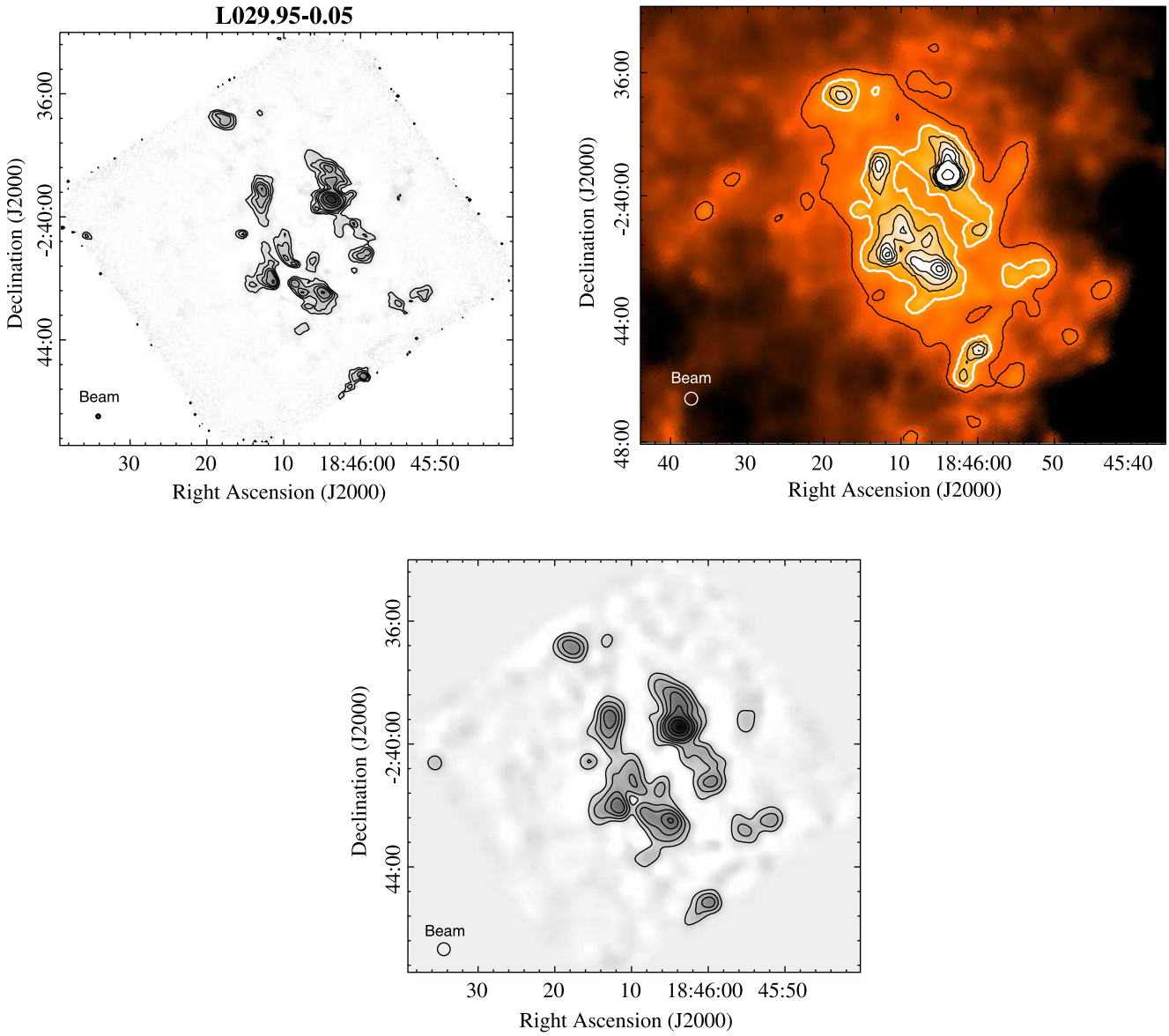

Figure 14. Example of the 350 μm continuum emission from SHARC-II (upper left) and *Herschel*/SPIRE (upper right) toward the region $l = 28.^{\circ}95$, $b = -0.^{\circ}05$. Beam sizes are shown in the bottom left corner of each map. The contours of the SHARC-II image correspond to 3σ, 6σ, 10σ, 15σ, 30σ, 50σ, and 100σ, with an rms noise $\sigma = 514$ mJy beam^{-1}. Contours of the *Herschel* image start from 10σ, with increasing steps of 5σ ($\sigma = 164$ MJy sr^{-1}). The smaller beam size of SHARC-II images allow us to recover structures not identified by *Herschel* with lower resolution. Bottom: SHARC-II image convolved to match the 24.″9 FWHM beam size of *Herschel* image. Contours represent 1, 3, 6, 10, 15, 30, and 50 times the rms noise of the image. The 1σ contour level resembles the emission observed at the 15σ white contour level of the *Herschel* image. The 15σ level in the *Herschel* map sets then a limit of the diffuse emission filtered out in the SHARC-II maps (see Section 4.7).

dust temperatures of the rest of the clumps have an average of 27 K, and a median of 29 K. Thus, the parameters that we found in sources with strong (>1 Jy) integrated emission at 1.1 mm are similar to those found with SED fitting, giving some confidence to our values based on only two wavelengths. In addition, BGPS clumps associated with massive star-forming regions generally have strong emission at mm and submm wavelengths, with warm temperatures ~30 K, lying above 89% of the distribution of fitted temperatures of BGPS sources with T ⩽ 50 K.

Battersby et al. (2011) used Hi-GAL 70–500 μm data to identify significant dust continuum emission in two $2^{\circ} \times 2^{\circ}$ regions centered at $l = 30^{\circ}$ and $l = 59^{\circ}$, and obtained temperature and column density maps for them by fitting SEDs for each pixel. While the temperature is a free parameter for their fitting model, the spectral index is fixed to 1.75 following Ossenkopf & Henning (1994). From our sample, we have 91 BGPS V2.1 sources with determined temperatures in the $l = 30^{\circ}$ map, and none in the $l = 59^{\circ}$ map. Considering $T_{\rm SHARC}$ the fitted temperature obtained from Equation (1), the median and average temperature for those sources from our analysis is 18 K and 34 ± 4 K for $\beta = 1.7$. We estimated a value of the temperature of these sources from the maps presented by Battersby et al., $T_{Herschel}$, averaging the temperature values of each pixel on an aperture of 40″ centered on the peak position of each source. Figure 19 shows the ratio $T_{\rm SHARC}/T_{Herschel}$ as a function of the flux density at 1.1 mm for the sample of BGPS sources. The average ratio from this figure, without considering those sources with $T_{\rm SHARC} > 50$ K for which the uncertainties are much larger, is 0.83 ± 0.05, while the weighted mean is 0.50 ± 0.01.

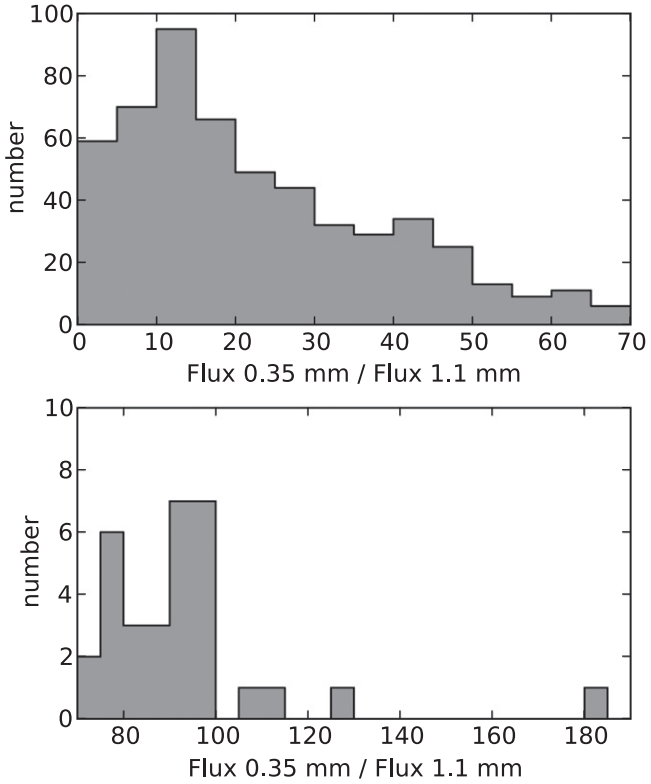

Figure 15. Distribution of the flux ratio between the emission at 0.35 and 1.1 mm for our sample of 574 BGPS V2.1 sources with reliable flux values. Nearly 94% of the sources have a flux ratio lower than 70.2.

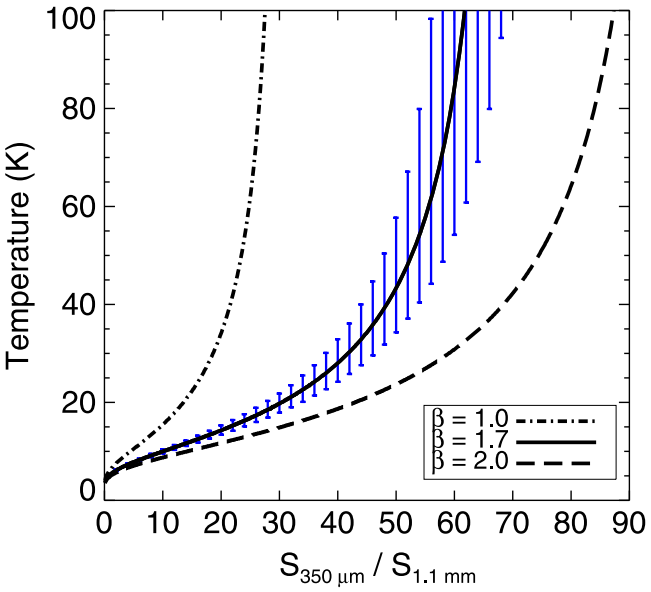

Figure 16. Models of dust temperature as a function of the flux ratio between continuum emission at 350 μm and 1.1 mm, in the optically thin limit. The three models correspond to different opacity laws, $\beta = 1.0$, $\beta = 1.7$, and $\beta = 2.0$. The error bars for the $\beta = 1.7$ model show the expected uncertainty in temperature determination when the flux ratio has an error of 10%.

To identify dense material associated with the formation of massive stars and clusters, Battersby et al. (2011) performed iterative removal of cirrus cloud emission on Hi-GAL images. The spectral emission distribution fitted for each point across

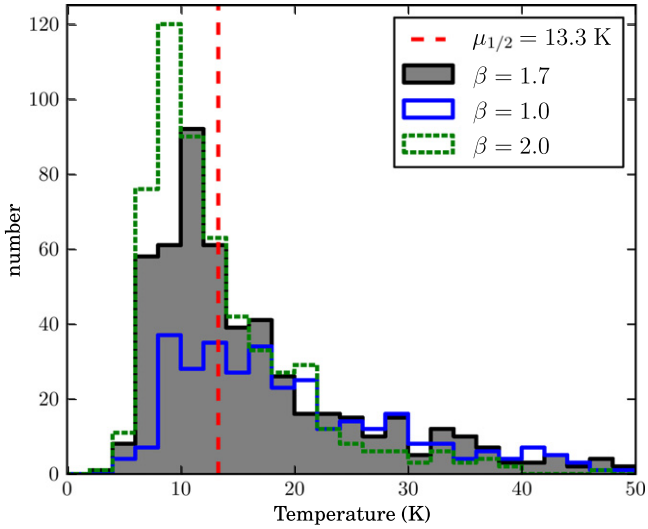

Figure 17. Distribution of temperatures of the BGPS sources with good fit in the determination of temperature, using the three different opacity models: spectral index $\beta = 1.0$ (blue line), $\beta = 2.0$ (green dashed line), and $\beta = 1.7$ (shaded black line). The vertical red dashed line at $T = 13.3$ K represents the median value for the distribution with $\beta = 1.7$.

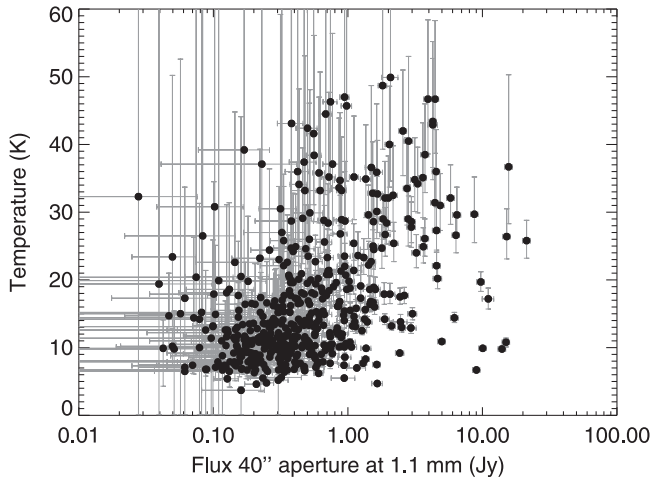

Figure 18. Temperature determined for the BGPS sample of sources as a function of their 40″ aperture flux, for a spectral index $\beta = 1.7$. Only sources with good fits in the determination of temperature ($T \leqslant 50$ K) are shown in this figure. There are few BGPS sources with high flux ($F_{1.1\ \mathrm{mm}} > 4$ Jy) and low temperature ($T < 20$ K); a description of them is presented in Section 5.1.

the map results in a median value for temperature of T = 23 K for a spectral index of $\beta = 1.7$ on $l = 30°$. The region considered as source emission is roughly the contour at 6.5σ ($\sim$1070 MJy sr^{-1}) in the 350 μm SPIRE band, and hence SHARC-II maps still miss extended emission that is considered to be source emission by Battersby et al. From their temperature map we estimated a temperature for this extended background emission, masking the region above 15σ from the 350 μm SPIRE map and also masking circular areas of 80″ diameter centered on each BGPS V2.1 source on the map. We found a temperature of 25 K, for a fixed $\beta = 1.75$ for the emission considered for SED fitting by Battersby et al. but filtered out in SHARC-II maps.

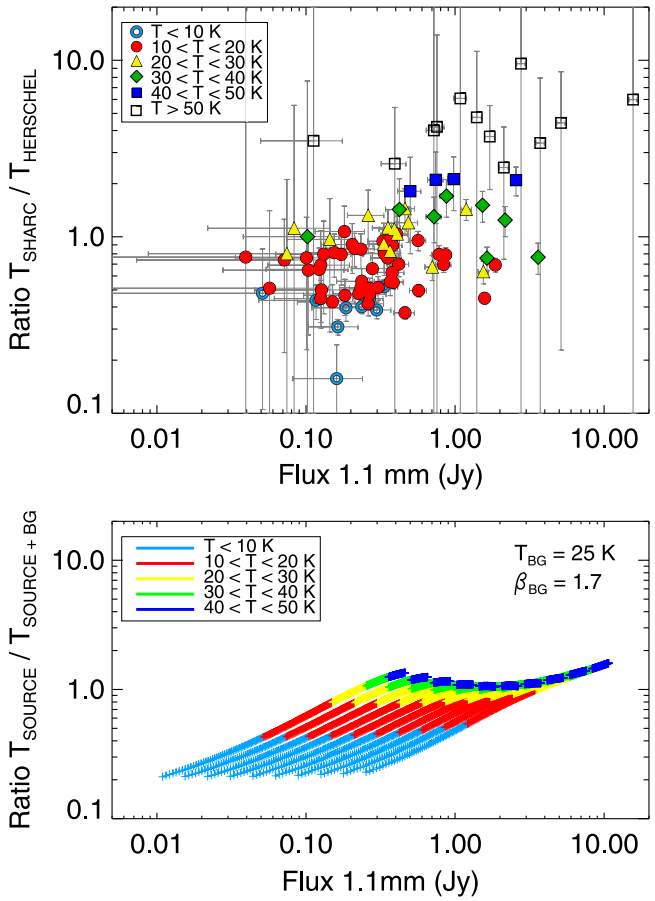

Figure 19. Upper: comparison between estimated temperatures with 350 μm and 1.1 mm continuum maps, $T_{\rm SHARC}$, and temperatures obtained from SED fitting by Battersby et al. (2011), $T_{Herschel}$, as a function of 40″ aperture flux density at 1.1 mm for a sample of 91 BGPS sources toward $l = 30°$. The colors shown in the legend represent different ranges for $T_{\rm SHARC}$. The mean value of the ratio, weighted by errors, is 0.50 ± 0.01 for sources with $T_{\rm SHARC} \leqslant 50$ K. Bottom: simulated recovery of sources immersed in a uniform background emitting as a modified blackbody with temperature $T_{\rm bg} = 25$ K, and spectral index $\beta = 1.7$. The input sources have temperatures and spectral index in the ranges $5 < T_{\rm source} < 50$ K, and $1.5 < \beta_{\rm source} < 2.5$, which are characteristic of clump-like features. The temperature ratio $T_{\rm source}/T_{\rm source+bg}$ of simulated sources immersed in background reproduce qualitatively the observed ratio $T_{\rm SHARC}/T_{Herschel}$ of the upper panel.

We then tested the estimation of color temperature on compact sources, if additional background emission were considered. A simple model of a source emitting uniformly as a modified blackbody, characterized by a temperature $T_{\rm source}$ and a spectral index $\beta_{\rm source}$, combined with background emission, also modeled as a modified blackbody, with $T_{\rm back}$ and $\beta_{\rm back}$. The measured fluxes of the composite emission, $S_{350\,\mu{\rm m}}$ and $S_{1.1\,{\rm mm}}$, correspond to the sum of individual contributions at those wavelengths, and following Equation (1), differences between $T_{\rm source}$ and $T_{\rm back}$ and $\beta_{\rm source}$ and $\beta_{\rm back}$, will recover a new set of measured values T_M and β_M. For a field near $l = 30°$, where the very dense structures are likely spread over diffuse emission with $T_{\rm back} = 25$ K and $\beta_{\rm back} = 1.7$, we simulated the recovery of properties for input sources with a range of parameters characteristic of clump-like features, $5 < T_{\rm source} < 50$ K, and $1.5 < \beta_{\rm source} < 2.5$. The ratio $T_{\rm source}/T_{\rm source+bg}$ of the input to the determined temperatures, as

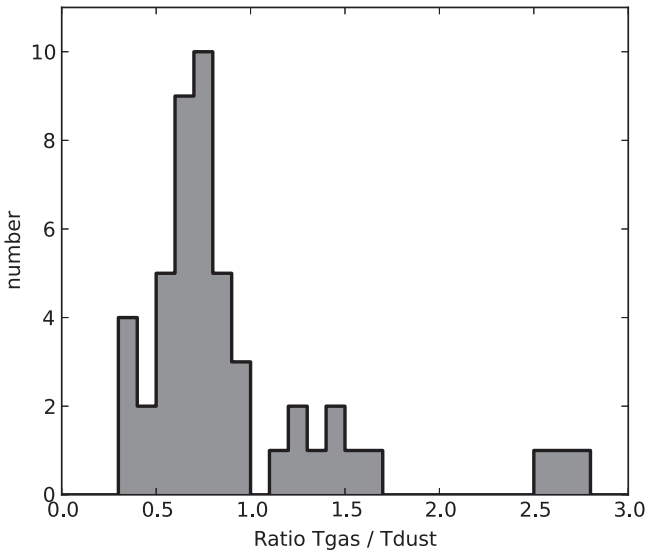

Figure 20. Distribution of the ratio of gas temperature determined from NH_3 observations $T_{\rm gas}$, and fitted dust temperatures $T_{\rm dust}$, for the sample of 49 BGPS sources with $T_{\rm gas} < 30$ K and $T_{\rm dust} < 50$ K, ranges in which both values are relatively well determined. The average and median values of this distribution are 0.88 and 0.76, respectively.

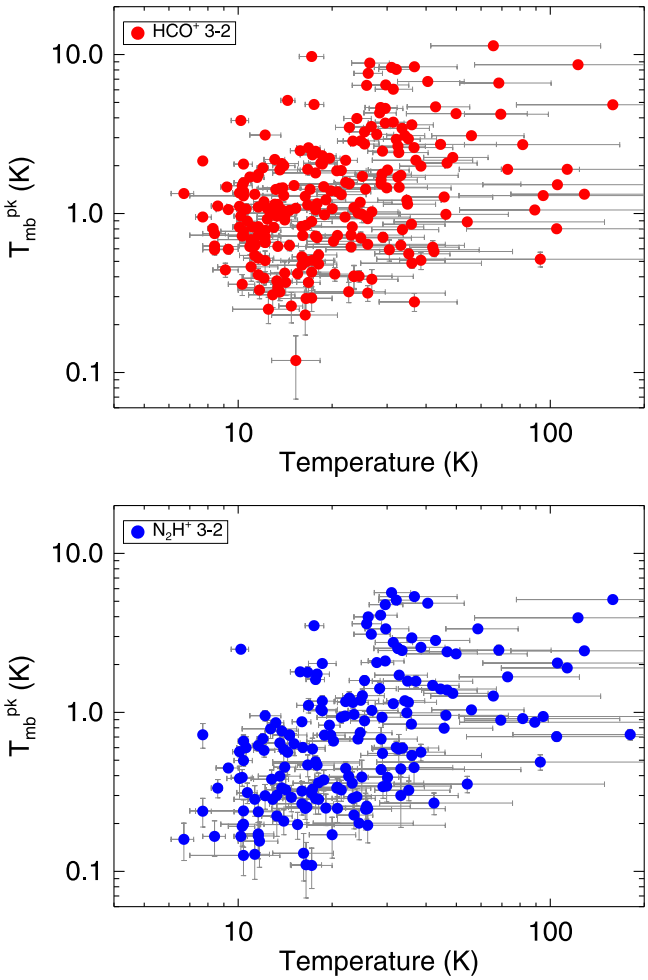

Figure 21. Peak main-beam temperature, as a function of dust temperature, for the sample of BGPS sources from the spectroscopy catalog by Shirley et al. 2013 that are contained in the SHARC-II maps. The number of sources with HCO^+ emission is 250, and the number of sources with N_2H^+ emission is 199.

a function of the measured 1.1mm flux, are shown in the lower panel of Figure 19. The results are qualitatively similar to the comparison between $T_{\rm SHARC}$ and $T_{Herschel}$, with low-flux, cold sources having low ratios of temperatures; warm, strong mm emission clumps have ratios of temperatures slightly above 1.0; and with sources with temperatures of 10–20 K (the bulk of BGPS clumps in $l = 30°$) with temperature ratios in the range 0.4–1.0.

A more direct comparison can be performed with compact sources extracted on *Herschel* images using the CUTEX method, designed for detection of sources on intense and highly variable foreground/background (Molinari et al. 2011). Using a similar method as that presented by Elia et al. (2013), a catalog of extracted compact sources and their associated physical parameters, using the five bands of Hi-GAL, have been obtained for the inner Galaxy ($-70° < l < 67°$) (D. Elia et al. 2015, in preparation). These sources are extracted from background emission and therefore considered to represent the very dense clump-core features across molecular clouds. From a simple spatial match performed to the 102 BGPS sources toward $l = 30°$ that have estimated color temperatures, 76 of these clumps have a counterpart Hi-GAL compact source, and preliminary results produce much better agreement with the temperatures derived in this paper from SHARC and BGPS data; the ratio between these temperatures has a mean of 1.05 and a median of 0.97. In both cases, a fixed value of the spectral index $\beta = 2.0$ was considered. Several considerations need to be assessed, such as different beam resolutions between observation bands, and a more complete analysis between the presented sample of SHARC-II maps and properties of extracted sources with Hi-GAL, including substructures and association with emission at 70 μm, will be the subject of a forthcoming work.

5.3. Comparison between Gas Temperature from NH_3 and Color Temperature

Figure 20 shows the ratio of gas to dust temperatures for a sample of BGPS sources. The gas temperatures were determined from NH_3 observations (Dunham et al. 2010; Wienen et al. 2012 and BGPS team 2015, in preparation). For those observations not centered on peak positions of BGPS sources, we associated the NH_3 detections to their closest BGPS source within one beam distance. Only the 49 clumps with dust temperatures below 50K and gas temperatures below 30 K are plotted. The ratio $T_{\rm gas}/T_{\rm dust}$ has a weighted average of 0.88 and a median of 0.76. There are few sources with equal temperatures, but instead a group with lower $T_{\rm gas}$ and a group with higher $T_{\rm gas}$.

5.4. Comparison with Tracers of Dense Gas

Schlingman et al. (2011) presented spectroscopic observations of HCO^+ and N_2H^+ (3–2) for 1882 sources from BGPS. The selection of sources was made between Galactic longitudes $10° \leqslant l \leqslant 90°$, considering all sources with integrated flux in a 40″ aperture greater than $S_{1.1\,\rm mm} \sim 0.4$ Jy, and from bins of logarithmically spaced flux of 0.1 for sources with $S_{1.1\rm mm} = 0.1$–0.4 Jy. A new, complete version of this catalog by Shirley et al. (2013) includes all 6194 sources in the BGPS V1.0 catalog between $7.°5 \leqslant l \leqslant 194°$ of this pair of molecular transitions. After considering a one-to-one match between sources from V1.0 and V2.1 catalogs, with a spatial matching of one beam of distance (33″), we checked which of those sources are present in our sample of SHARC-II maps. There are 300 V2.1 sources with spectroscopy data, 250 of them with HCO^+ detections and estimated dust temperatures from our analysis, and 199 with N_2H^+ detections with dust temperatures. Figure 21 shows the peak main beam temperature versus our fitted temperature for that group of sources. The points scatter widely about the plot. Considering only the sources with dust temperatures less than 50 K (169 for N_2H^+ and 223 for HCO^+), the Spearman's rank correlation coefficient of the distributions of $\log(T_{\rm mb}^{\rm pk})$ and $\log(T_{\rm dust})$ are 0.51 for sources with N_2H^+ detections and 0.33 for sources with HCO^+ detections. We tested the null hypothesis of no significant correlation between $\log(T_{\rm mb}^{\rm pk})$ and $\log(T_{\rm dust})$ for these distributions. For a sample size n, the Student's t value for the Pearson correlation coefficient $r(n)$ is estimated from $t = r/s_r$, with $s_r = \sqrt{(1 - r^2)/(n - 2)}$. For a two-tailed probability value $p = 0.05$, our sample requires $t = 2$, corresponding to $r(169) = 0.151$ and $r(223) = 0.131$. The estimated values for the correlation coefficients of our sample are $r = 0.508$ and $r = 0.332$ for N_2H^+ and HCO^+, respectively, rejecting the null hypothesis at a 95% confidence. Therefore, although the correlation is weak, in both cases it is statistically significant for the detected peak main beam temperature and the fitted dust temperature. In the case of N_2H^+, the correlation can be fitted as $\log(T_{\rm mb}^{\rm pk}) = {\rm B} \times \log(T_d) + {\rm A}$, with fitted values A = −1.55 and B = 1.04 ± 0.13. For HCO^+, the fitted parameters are A = −0.59 and B = 0.52 ± 0.08.

Shirley et al. (2013) suggested that BGPS sources with a higher N_2H^+/HCO^+ ratio could be clumps with dense core-like structures in them, as a consequence of cold, CO-depleted gas within those cores. Nevertheless, we did not find a clear correlation between the ratio of high density tracers N_2H^+/HCO^+, and number of substructures or estimated dust temperature in our source sample. Parental clumps with large multiplicity of substructures and high N_2H^+/HCO^+ ratios represent good candidates for future interferometric observations to study core properties in regions of clustered massive-star formation.

6. DISCUSSION

6.1. Mass and Surface Density of Substructures

We use the following equation to calculate the mass:

$$M_d = \frac{S_\nu D^2}{\kappa_\nu B_\nu(T_d)}, \quad (2)$$

where S_ν is the flux density, D is the distance to the source, and κ_ν is the dust mass opacity coefficient.

We use a dust opacity of 1.14 $\rm cm^2 g^{-1}$ of dust at 1.1 mm (Ossenkopf & Henning 1994) for a model with thin ice mantles (OH5). Assuming a dust-to-gas mass ratio of $R = M_d/$

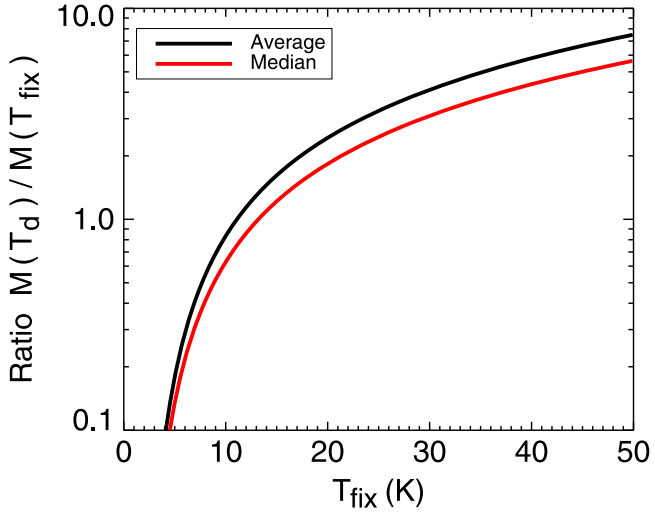

Figure 22. Ratio between the mass estimated using color temperatures determined from 350 μm and 1.1 mm images ($T_{\rm clump}$), and the mass estimated using a single fiducial temperature ($T_{\rm fix}$). For the sample of 514 V2.1 BGPS sources with good fits in the determination of temperature, using $T_{\rm fix} = 20$ K, the average value of the source masses will be underestimated by a factor of ~2.4.

$M_g = 0.01$, the mass of gas and dust will be given by:

$$M_{1.1\,\rm mm} = 14.26\left(\frac{S_\nu}{Jy}\right)\left(\frac{1.14\ \rm cm^2\ g^{-1}}{\kappa_{1.1\,\rm mm}}\right)\left(\frac{D}{\rm kpc}\right)^2 \times\left\{\exp\left(\frac{13.01}{T_d}\right)-1\right\}M_\odot. \quad (3)$$

From our sample of 512 BGPS sources with temperatures $\leqslant$50 K, we can give some estimates of how the values of masses will change when a fixed temperature is used. The average ratio between the clump mass $M(T_d)$, with T_d the fitted dust temperature from continuum observations between 350 μm and 1.1 mm, and the mass estimated at a fixed temperature, $M(T_{\rm fix})$, is obtained from:

$$\left\langle\frac{M(T_d)}{M(T_{\rm fix})}\right\rangle = \left\langle\frac{\exp\left(13.01/T_d\right)-1}{\exp\left(13.01/T_{\rm fix}\right)-1}\right\rangle. \quad (4)$$

Figure 22 shows the results of the above equation for different values of $T_{\rm fix}$. For simplicity it is common to use a fixed value of 20 K in determination of masses from millimeter surveys of Galactic star-forming regions (e.g., Motte et al. 2007; Schlingman et al. 2011; Urquhart et al. 2013). Using $T_{\rm fix} = 20$ K, the average value of the ratio is 2.43 ± 0.11, with a median value of 1.83. Therefore, assuming a fiducial value for the temperature of 20 K for our sample of clumps, the estimation of masses would be underestimated on average, with respect to the mass obtained from our analysis of color temperatures.

From Ellsworth-Bowers et al. (2013, 2015), kinematic distances were determinal for a large number of BGPS sources. Only a fraction of our sample of BGPS clumps have estimated distances, so we cannot calculate masses for the entire group. However, we can estimate the contribution of masses from substructures detected at 350 μm with respect to the parental clump, because both substructures and clump are located at the same distance. We use the flux density at 350 μm to compute masses of the substructures. Similar to Equation (3), but with appropriate change in the exponential and with a dust opacity of 11 $\rm cm^2 g^{-1}$ (OH5), the mass measured at 350 μm is as follows:

$$M_{350\,\mu\rm m} = 0.053\left(\frac{S_\nu}{Jy}\right)\left(\frac{11\ \rm cm^2\ g^{-1}}{\kappa_{350\,\mu\rm m}}\right)\left(\frac{D}{\rm kpc}\right)^2 \times\left\{\exp\left(\frac{41.14}{T_d}\right)-1\right\}M_\odot \quad (5)$$

From our sample of 349 BGPS parental clumps associated with 1352 high-resolution sources, the fraction of the total mass estimated for structures at 350 μm with respect to the mass of

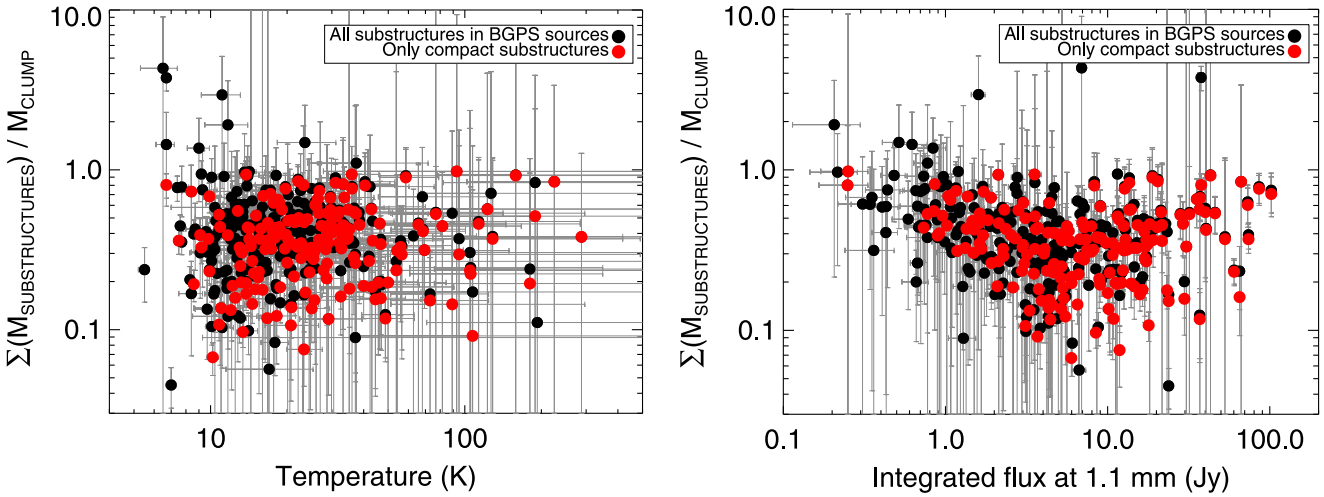

Figure 23. Comparison between the total estimated mass from 350 μm substructures in each clump, and the mass estimated at 1.1 mm for that parental BGPS clump, as a function of dust temperature (left) and the integrated flux of the BGPS sources (right). Black points consider for $M_{\rm substructures}$ the flux contribution from all high-resolution sources in the parental clumps, and have a weighted averaged mass fraction $\sum(M_{\rm substructures})/M_{\rm clump}$ of 0.22 ± 0.01. Red points only consider the flux contribution from strong, compact substructures, and the averaged mass fraction, weighted by errors, of this distribution is 0.19 ± 0.01.

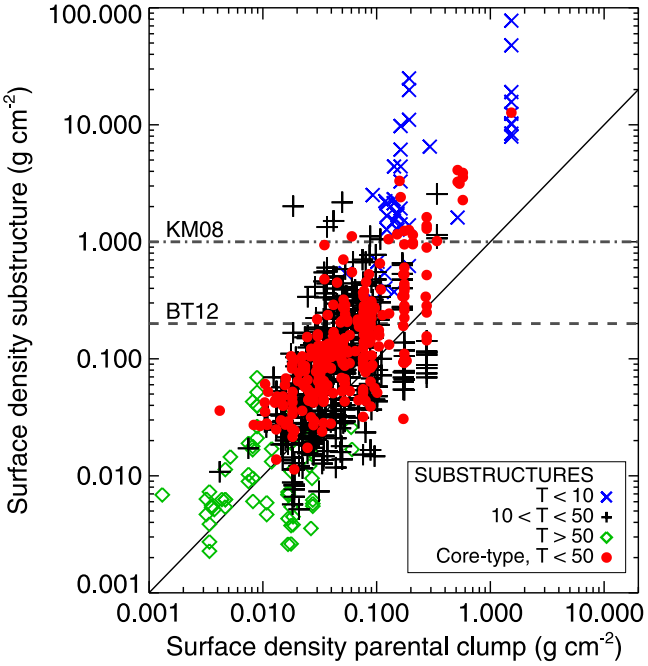

Figure 24. Estimation of surface density between substructures and parental clumps. Solid line represent the locus of equality between the structures. Black crosses show the bulk of the sources, with temperatures between 10–50 K. Blue marks show sources with low temperature ($T < 10$ K), likely to overestimating the surface density. Gray marks show sources with high temperature ($T > 50$ K). Red points show only those compact, core-type substructures found in the parental clumps, with detections above 10σ. Most of these compact sources have higher surface 2–3 times larger than their parental clump. Several of these compact sources have surface densities above theoretical thresholds of 0.2 g cm^{-2} (Butler & Tan 2012) or 1.0g cm^{-2} (Krumholz & McKee 2008) for massive star formation (see Section 6.1).

the parental 1.1 mm clump is determined by:

$$\frac{\sum(M_{\rm substructures})}{M_{\rm clump}} = 3.75 \times 10^{-3}\left(\frac{S^{*}_{350\mu m}}{S^{*}_{1.1mm}}\right) \times \left(\frac{\exp\left(41.14/T_d\right)-1}{\exp\left(13.01/T_d\right)-1}\right), \quad (6)$$

where $S^{*}_{1.1\ \rm mm}$ is the emission of the parental BGPS clump and $S^{*}_{350\,\mu\rm m}$ represent the total emission of substructures inside that clump. We consider the same dust temperature T_d, fitted from Equation (1), for substructures and their parental clump. Here the integrated emission recovered by *Bolocat* for each clump is taken into account, which estimates the total flux for the area delimited by the *labelmask* region (see Section 4.5). In that way, the contribution of each substructure will be associated with a single parental clump, with both considered at the same dust temperature.

Figure 23 shows the ratio between masses obtained for high-resolution sources at 350 μm and their parental BGPS clump, as a function of the dust temperature and as a function of the integrated flux at 1.1 mm. Black points represent the mass ratio considering the flux contribution of all high-resolution sources, and red points only consider emission from strong, compact sources. The average and median values for the mass ratio $\sum(M_{\rm substructures})/M_{\rm clump}$ when all substructures are considered, are 0.48 and 0.40, respectively, with a mean weighted by errors of 0.22 $\pm$ 0.01. Parental clumps that are more massive and colder have smaller uncertainties, so the mean mass ratio weighted inversely by uncertainty is smaller. When only compact substructures (see Section 4.5) are considered, the average and median of the distribution are 0.39 and 0.37, respectively, with a mean weighted by errors of 0.19 $\pm$ 0.01. These results for the mass fraction are larger than the results from Ragan et al. (2013), who fit SEDs and obtained a value of $\sim$14% for the mass contribution of core-like features observed at a resolution of 7.″8 compared to the total mass of their harboring IRDCs. Possible explanations of this difference are our larger sample of sources (Ragan et al. consider 11 IRDCs, harboring a total of 83 substructures), and also that, contrary to BGPS sources, IRDCs are not limited to compact structures. Besides, our sample of clumps has a broader range of evolutionary stages, not necessarily limited to the coldest, initial stages of massive star formation, represented by the IRDC phase.

Assuming a uniform temperature will also introduce errors in the mass determination. The parental molecular clump will be affected by both embedded stars and the external radiation field, and it is likely that substructures will have a different temperature from their surrounding medium. In addition, SHARC-II and Bolocam are sensitive to different spatial scale emission (see Section 4.3), and therefore the recovered flux at 1.1 mm could include faint, extended background emission not detected in 350 μm continuum emission. A better analysis of the mass ratio between parental clumps and their internal structures (compact, core-type sources, and faint, filamentary emission) will require a comparison between SHARC-II and *Herschel* maps at 350 μm, or modeling these sources using radiative transfer codes.

Figure 24 shows the surface density $\Sigma_{350\,\mu\rm m}$ estimated for the substructures found in the 350 μm map, as a function of the surface density of their parental clump, $\Sigma_{1.1\ \rm mm}$. We considered the deconvolved radius of resolved substructures at 8.″5 and resolved clumps at 33″ Identified substructures have in general larger surface densities than their parental BGPS source. For the sample of spatially resolved sources, there are 418 compact substructures, 286 of which have estimated temperatures $T_d \leqslant 50$ K. These are represented by red points in the figure. A linear fit of the compact sources indicate that they have $\Sigma_{350\,\mu\rm m} \sim 2.2 \times \Sigma_{1.1\ \rm mm}$. Eighteen of them (6%) have $\Sigma_{350\,\mu\rm m} \geqslant 1.0$ g cm^{-2}, a theoretically predicted threshold for the formation of massive stars (Krumholz & McKee 2008). More recently a lower value of 0.2g cm^{-2} was proposed by Butler & Tan (2012) as the initial condition of massive star formation in the Galaxy; 88 (31%) of our sources meet that criterion.

Thus, for our sample of high-resolution structures observed at 350 μm, there are probably many dense cores, whose physical parameters suggest ongoing or imminent formation of massive stars.

6.2. Uncertainties on Determined Physical Parameters of Clumps

Following Equation (1), the presence of additional integrated flux densities observed at 350 μm and 1.1 mm not related to the dust emission of a given clump-like source, such as emission from the surrounding environment of the compact source, or contamination from molecular lines on those bands, can introduce dissimilarities between the

recovered and real flux ratio and therefore in subsequent derived physical parameters. As seen in Section 5.2, the temperature estimated for a source embedded in a background with different temperature (or spectral index) may differ from the actual source temperature. While the data-reduction pipeline of the Hi-GAL survey is coded to remove low frequency noise, which imply that the 350 μm Herschel images recover faint diffuse emission (Traficante et al. 2011), SHARC-II maps filter out most of that emission and recover the very dense, compact structures, and BGPS maps are not sensitive to extended emission at scales larger than 2′–3′ (Ginsburg et al. 2013). The precise amount of additional flux per band is determined by the temperature and spectral index of the background extended emission (see Figure 19).

In the case that observations of a particular clump recover some background emission in the 1.1 mm BGPS but not in the 350 μm SHARC-II maps, their overall effect would consist of lower measured color temperature and higher mass estimation. Contamination of CO(7 – 6) lines by the 350 μm emission is not expected for the bulk of clumps in this work. The $J = 7$ level of CO is 155 K above ground, and even though this line has been seen in sources with kinetic gas temperature of ~25 K (Krugel et al. 1989), emission is expected only in the warmer and denser clumps. No line contamination is possible at 1.1 mm since the passband of Bolocam excludes the strong CO(2 – 1) line.

To quantify these uncertainties, we consider two hypothetical cases of clumps with equal spectral index $\beta = 1.7$ and temperatures $T_{\rm source}$ of 20 K and 40 K, respectively. These sources have an associated value $R_{\rm source}$ of the ratio of integrated flux densities observed at 350 μm and 1.1 mm, and additional emission in these bands will produce variation of the measured value of the flux ratio, R_M. For the case $T_{\rm source} = 20$ K, differences of less than 20% between R_M and the intrinsic flux ratio of the source $R_{\rm source}$, will imply a measured temperature T_M also 20% different from the source temperature $T_{\rm source}$. From Equation (3), the uncertainty in the determination of the clump mass and surface density will be ~30%.

For warmer sources, even small changes to the flux ratio will result in large uncertainties in the measured T_M. For $T_{\rm source} = 40$ K, differences of 10% between R_M and $R_{\rm source}$ will result in differences of 30% of T_M with respect to $T_{\rm source}$, and clump mass and surface density will also have uncertainties ~30%. In the case of differences of 20% between R_M and $R_{\rm source}$, measured temperatures could be 80% different from the real $T_{\rm source}$, and clump mass and surface density will have additional uncertainties of ~50%.

7. SUMMARY AND CONCLUSIONS

We presented a set of 107 SHARC-II 350 μm maps toward star-forming clumps. Most of maps are observed toward sources from the BGPS V2.1 catalog, with additional maps covering three outer Galaxy star-forming regions. The maps have a resolution of 8.″5, improving upon the resolution of the BGPS maps at 1.1 mm (33″) and revealing a population of substructures.

We used *Bolocat* to identify significant emission in the SHARC-II maps, and we obtained a catalog of 1386 high-resolution sources, with average fluxes of 23.15 ± 1.59 Jy and average radius of 15″ We found that ~32% of these features have peak emission above $10\sigma_{\rm rms}$, and we consider these "compact substructures" as core-like sources immersed in parental clumps. Below this limit, recovered sources are called "faint substructures," and they are related with fragmentation of filamentary features, isolated low intensity sources, and residuals from the source extraction algorithm.

We found 619 BGPS V2.1 sources in our set of 350 μm maps, only 56% of which are associated with 1352 high-resolution substructures. While most of the parental clumps have only one or two associated substructures, we found significant multiplicity in some of them, with 22 clumps having more than 10 substructures in them.

We compared the 350 μm continuum emission from SHARC-II maps with *Herschel* images from the Hi-GAL survey toward the $l = 30°$ region at same wavelengths. Strong emission detected in SHARC-II maps is in general in good agreement with the *Hershel* fluxes, but faint sources from the SHARC-II maps are immersed in background emission.

We estimated temperatures for different models of the spectral index. For the 512 sources with "good fits" in the determination of temperatures ($T_d \leqslant 50$ K), the median and average values of their temperatures are 13.3 K and 16.3 ± 0.4 K, respectively, in reasonable agreement with other temperature determination methods based on SED analysis.

Comparison to gas temperatures derived from NH_3 observations reveals sources with ratios of $T_{\rm gas}/T_{\rm dust}$ both larger and smaller than unity, but with mean value of 0.88.

Sources with N_2H^+ and HCO^+ detections present weak correlations between their observed peak main beam temperature and their fitted dust temperature. There is no clear correlation between the ratio $T_{\rm mb}^{\rm pk}(N_2H^+)/T_{\rm mb}^{\rm pk}(HCO^+)$ and the number of substructures found on parental clumps.

The fraction of the mass contained in substructures compared with the total parental clump mass has an average of 0.48, but this value decreases to 0.22 when weighted by uncertainties. Considering only the compact structures, likely to be core sources, the mass fraction between substructures and parental clumps is 0.19, higher than other studies of high angular resolution at 350 μm.

Small, but significant fractions of substructures satisfy theoretical thresholds for massive star formation of 0.2 (31%) or 1.0 (6%) g cm^{-2}.

We thank the anonymous referee for the helpful comments and suggestions that improve the clarity of this article. We would like to thank all the people involved in obtaining our observations including D. Dowell, students and researchers from the University of Texas, and staff from CSO. The BGPS project was supported in part by the National Science Foundation through NSF grant AST-0708403. The first observing runs for BGPS were supported by travel funds provided by NRAO. Support for the development of Bolocam was provided by NSF grants AST-9980846 and AST-0206158. N.J.E. and M.M. were supported by NSF grant AST-1109116. MM was also supported by a Fulbright Fellowship. This material is based upon work at the Caltech Submillimeter Observatory, which is operated by the California Institute of Technology under cooperative agreement with the National Science Foundation (AST-0838261). Herschel Hi-GAL data processing, maps production and source catalogue generation from the Hi-GAL Team have been possible thanks to Contracts I/038/080/0 and I/029/12/0 from ASI, Agenzia Spaziale Italiana. Herschel in an ESA space observatory with science

instruments provided by European-led Principal Investigator consortia and with important participation from NASA. SPIRE has been developed by a consortium of institutes led by Cardiff Univ. (UK) and including Univ. Lethbridge (Canada); NAOC (China); CEA, LAM (France); IAPS, Univ. Padua (Italy); IAC (Spain); Stockholm Observatory (Sweden); Imperial College London, RAL, UCL-MSSL, UKATC, Univ. Sussex (UK); Caltech, JPL, NHSC, Univ. Colorado (USA). This development has been supported by national funding agencies: CSA (Canada); NAOC (China); CEA, CNES, CNRS (France); ASI (Italy); MCINN (Spain); Stockholm Observatory (Sweden); STFC (UK); and NASA (USA).

APPENDIX A
CALIBRATIONS

Table 6 presents in detail the flux calibration and the observed values of τ at 225 GHz for each observation run. Flux conversion factors for one beam ($C_{\rm beam}$), 20″ and 40″ aperture conversion factors on SHARC-II maps (C_{20} and C_{40}), and

Table 6
Calibrators

Date	Calibrator	$\tau_{225\ \rm GHz}$	$C_{\rm beam}$ (Jy beam^{-1} μV^{-1})	C_{20} (Jy μV^{-1})	C_{40} (Jy μV^{-1})	$C_{40}^{33''}$ (Jy μV^{-1})
2006 Jun 11	Mars	0.071	10.86	0.39	0.31	0.46
	Mars	0.071	10.15	0.42	0.30	0.46
	Mars	0.071	11.63	0.40	0.33	0.49
2006 Jun 23	Uranus	0.061	8.55	0.28	0.24	0.36
	Uranus	0.062	8.02	0.28	0.23	0.34
2007 Jul 9	Mars	0.068	7.56	0.27	0.22	0.33
	Uranus	0.058	6.55	0.22	0.18	0.27
	Uranus	0.068	7.57	0.25	0.21	0.31
	Neptune	0.058	6.76	0.22	0.19	0.28
	Neptune	0.064	6.42	0.21	0.18	0.27
	Neptune	0.060	7.18	0.23	0.20	0.30
2007 Oct 24	Uranus	0.053	7.80	0.26	0.22	0.32
	Uranus	0.053	8.02	0.27	0.23	0.34
	Neptune	0.055	9.29	0.31	0.26	0.39
	Neptune	0.055	9.20	0.30	0.26	0.38
2007 Oct 27	Uranus	0.052	7.18	0.23	0.20	0.30
	Uranus	0.047	7.80	0.25	0.22	0.33
	Uranus	0.047	7.29	0.24	0.20	0.30
2009 Sep 10	Uranus	0.055	5.80	0.19	0.16	0.24
	Mars	0.062	6.31	0.23	0.18	0.27
2009 Dec 13	Uranus	0.050	6.34	0.22	0.18	0.26
	Uranus	0.050	6.13	0.23	0.18	0.26
	Mars	0.065	5.73	0.20	0.17	0.24
	Mars	0.065	5.67	0.20	0.16	0.24
2009 Dec 14	Uranus	0.068	6.01	0.22	0.17	0.25
	Mars	0.058	5.28	0.22	0.16	0.24
2009 Dec 29	Uranus	0.060	5.84	0.20	0.16	0.24
	Uranus	0.052	5.85	0.19	0.16	0.24
	Mars	0.062	5.72	0.22	0.17	0.26
	Mars	0.062	5.78	0.22	0.17	0.26
	Mars	0.056	5.80	0.22	0.17	0.26
2009 Dec 30	Uranus	0.050	7.06	0.24	0.19	0.28
	Uranus	0.051	7.08	0.24	0.19	0.28
	Mars	0.047	5.70	0.22	0.17	0.25
	Mars	0.052	5.68	0.22	0.17	0.25
	Mars	0.040	5.66	0.22	0.17	0.25
	Mars	0.040	5.81	0.24	0.18	0.26
2009 Dec 31	Uranus	0.051	6.43	0.22	0.18	0.27
	Uranus	0.049	6.32	0.22	0.18	0.26
	Uranus	0.050	6.26	0.22	0.18	0.27
	Mars	0.048	4.87	0.19	0.15	0.22
	Mars	0.048	4.79	0.20	0.15	0.22
2010 Jan 01	Mars	0.045	5.69	0.22	0.17	0.25
2010 Jul 24	Neptune	0.063	19.30	0.61	0.54	0.80
	Uranus	0.070	26.18	0.87	0.72	1.07
	Uranus	0.075	18.00	0.76	0.52	0.81
	Uranus	0.056	11.68	0.58	0.36	0.55
	Uranus	0.065	13.98	0.55	0.39	0.61
2010 Jul 25	Neptune	0.077	9.63	0.32	0.27	0.41
	Uranus	0.042	6.09	0.20	0.17	0.25
	Uranus	0.039	5.79	0.19	0.16	0.24

Table 6
(Continued)

Date	Calibrator	$\tau_{225\ \mathrm{GHz}}$	C_{beam} (Jy beam^{-1} μV^{-1})	C_{20} (Jy μV^{-1})	C_{40} (Jy μV^{-1})	$C_{40}^{33''}$ (Jy μV^{-1})
	Uranus	0.046	7.12	0.25	0.20	0.30
2010 Jul 28	Neptune	0.056	6.76	0.21	0.19	0.28
	Uranus	0.056	6.57	0.25	0.18	0.27
	Uranus	0.046	6.37	0.20	0.18	0.26
2010 Jul 31	Neptune	0.050	8.58	0.28	0.23	0.35
	Neptune	0.050	7.71	0.26	0.21	0.32
	Neptune	0.050	7.82	0.27	0.22	0.33
	Neptune	0.050	8.22	0.27	0.23	0.34
	Uranus	0.058	6.67	0.23	0.19	0.28
2010 Aug 01	Neptune	0.036	7.42	0.24	0.20	0.30
	Neptune	0.060	7.67	0.25	0.21	0.31
	Neptune	0.050	7.46	0.25	0.20	0.30
	Uranus	0.053	7.06	0.24	0.19	0.29
2010 Dec 05	Uranus	0.060	5.75	0.20	0.17	0.24
	Uranus	0.030	5.96	0.21	0.17	0.25
	Uranus	0.030	6.66	0.23	0.19	0.27
	Uranus	0.040	6.38	0.21	0.18	0.26
2010 Dec 06	Uranus	0.030	7.07	0.25	0.19	0.29
	Uranus	0.050	7.07	0.26	0.20	0.30
	Uranus	0.038	7.26	0.24	0.19	0.30
	Uranus	0.038	7.04	0.25	0.19	0.29
	Uranus	0.068	6.78	0.26	0.19	0.29
	Uranus	0.049	6.93	0.23	0.19	0.28
2011 Dec 23	Uranus	0.036	11.35	0.38	0.32	0.49
	Uranus	0.071	10.06	0.37	0.29	0.43
	Uranus	0.070	11.06	0.38	0.31	0.45
2012 Sep 14	Uranus	0.050	12.73	0.42	0.35	0.52
	Uranus	0.057	12.88	0.44	0.36	0.53
	Uranus	0.057	12.60	0.42	0.35	0.52
	Uranus	0.062	17.32	0.57	0.47	0.70
	Uranus	0.065	17.37	0.59	0.48	0.72
2012 Sep 21	Uranus	0.070	17.47	0.56	0.49	0.73
	Uranus	0.094	17.79	0.57	0.50	0.74
	Uranus	0.094	16.58	0.55	0.47	0.70

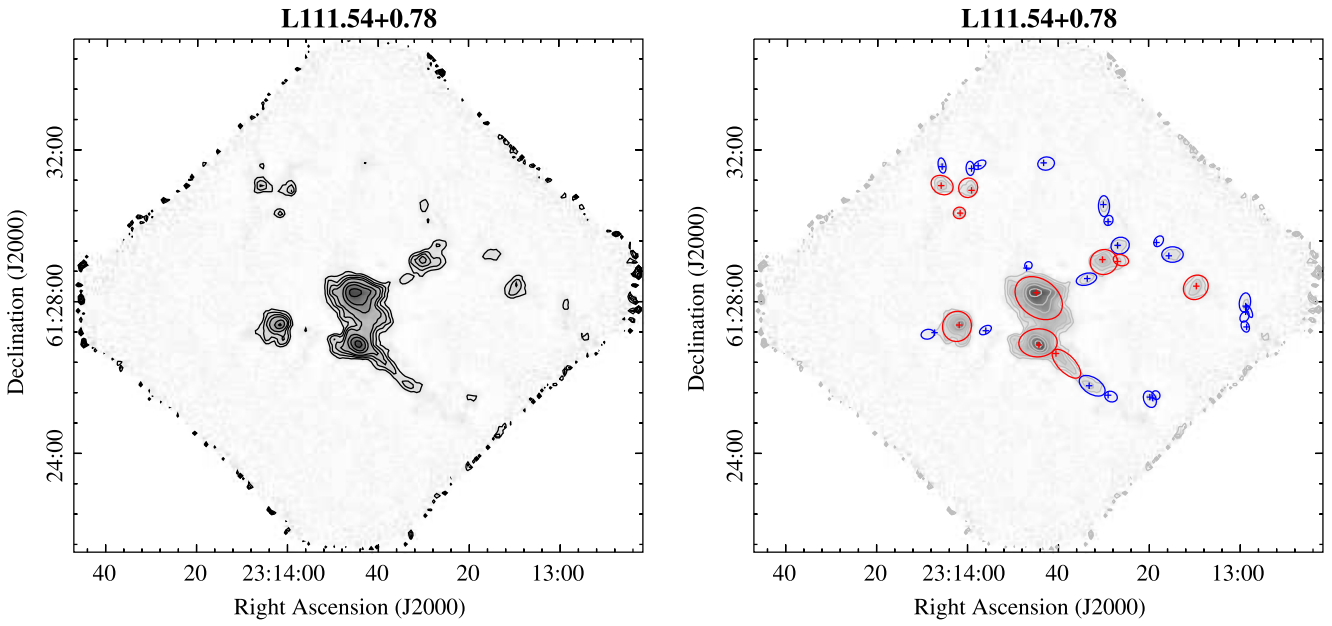

Figure 25. Continuum maps at 350 μm of the 107 regions included in our catalog. The beam size of the maps is 8.″5. Left: contours are drawn at 3σ, 6σ, 10σ, 15σ, 30σ, 50σ, and 100σ. Noise level σ_{rms} is indicated in the figure for each map. For the L111.54+0.78 map, σ_{rms} = 496 mJy beam^{-1}. Right: Recovery of substructures with *Bolocat* algorithm. Red and blue regions represent the position of dense, compact cores-type sources and faint substructures, respectively.

(The complete figure set (107 images) is available.)

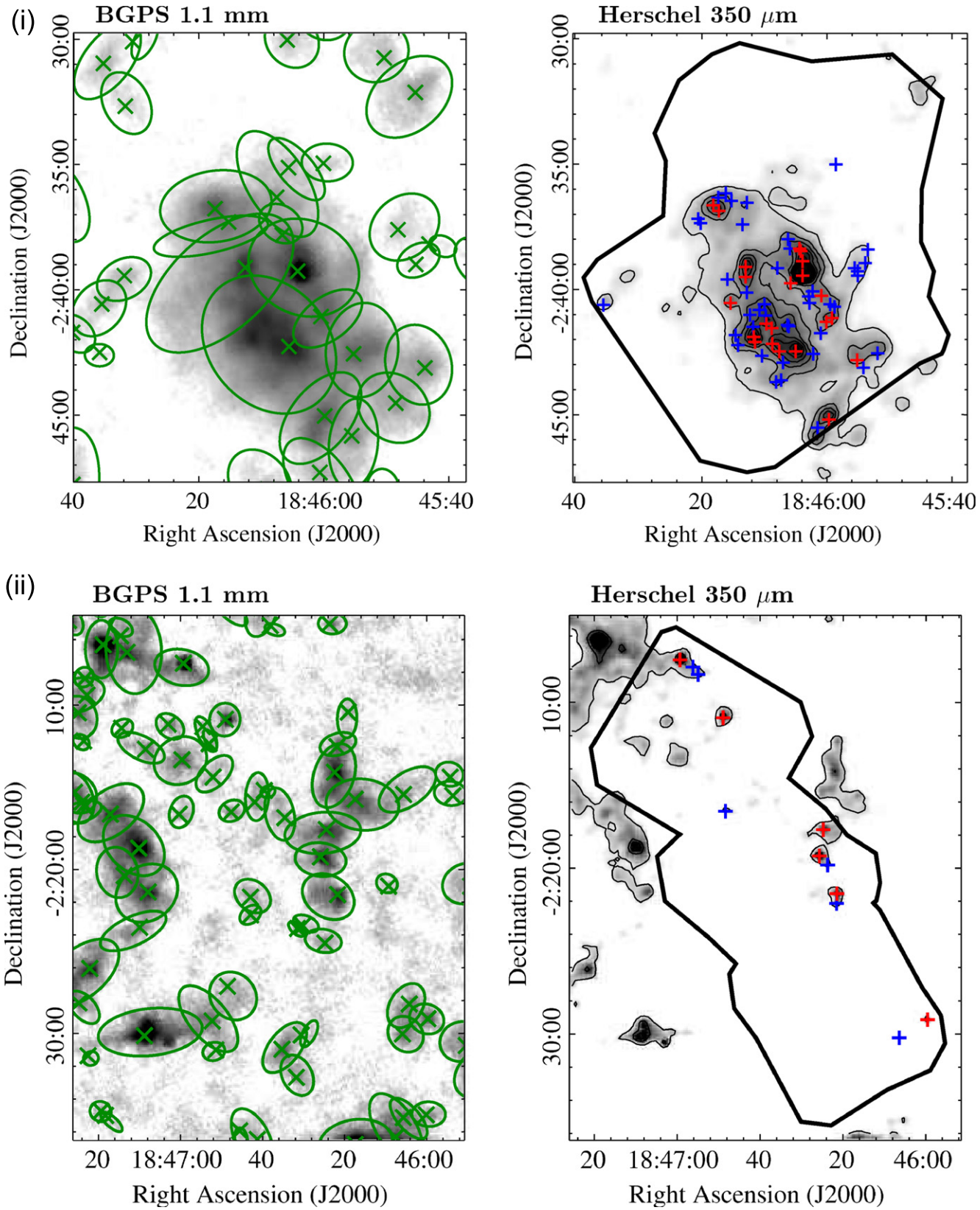

Figure 26. Left: BGPS map at 1.1 mm toward $l = 30°$. The ellipses show the recovered sources from the BGPS catalog. Right: Corresponding 350 μm maps from *Herschel* SPIRE. Contours start from 10σ, with increasing steps of 5σ ($\sigma = 164$ MJy sr^{-1}) The crosses show the peak position of the high-resolution sources recovered in SHARC-II map. Red and blue crosses show substructures with peak signal-to-noise above and below 10, respectively. (i) Thick black contour in Herschel map represents the area covered by SHARC-II maps L029.95-0.05 and L030.00+00. (ii) Thick black contour in Herschel map represents the area covered by maps L030.15+0.00, L030.30+0.00, and L030.45+0.00. (iii) Thick black contour in Herschel map represents the area covered by maps L030.60+0.00, L030.70-0.07 and L030.80-0.05. (iv) Thick black contour in Herschel map represents the area covered by map L030.88+0.13. (v) Thick black contour in Herschel map represents the area covered by map L030.61+0.16.

(An extended version of this figure is available.)

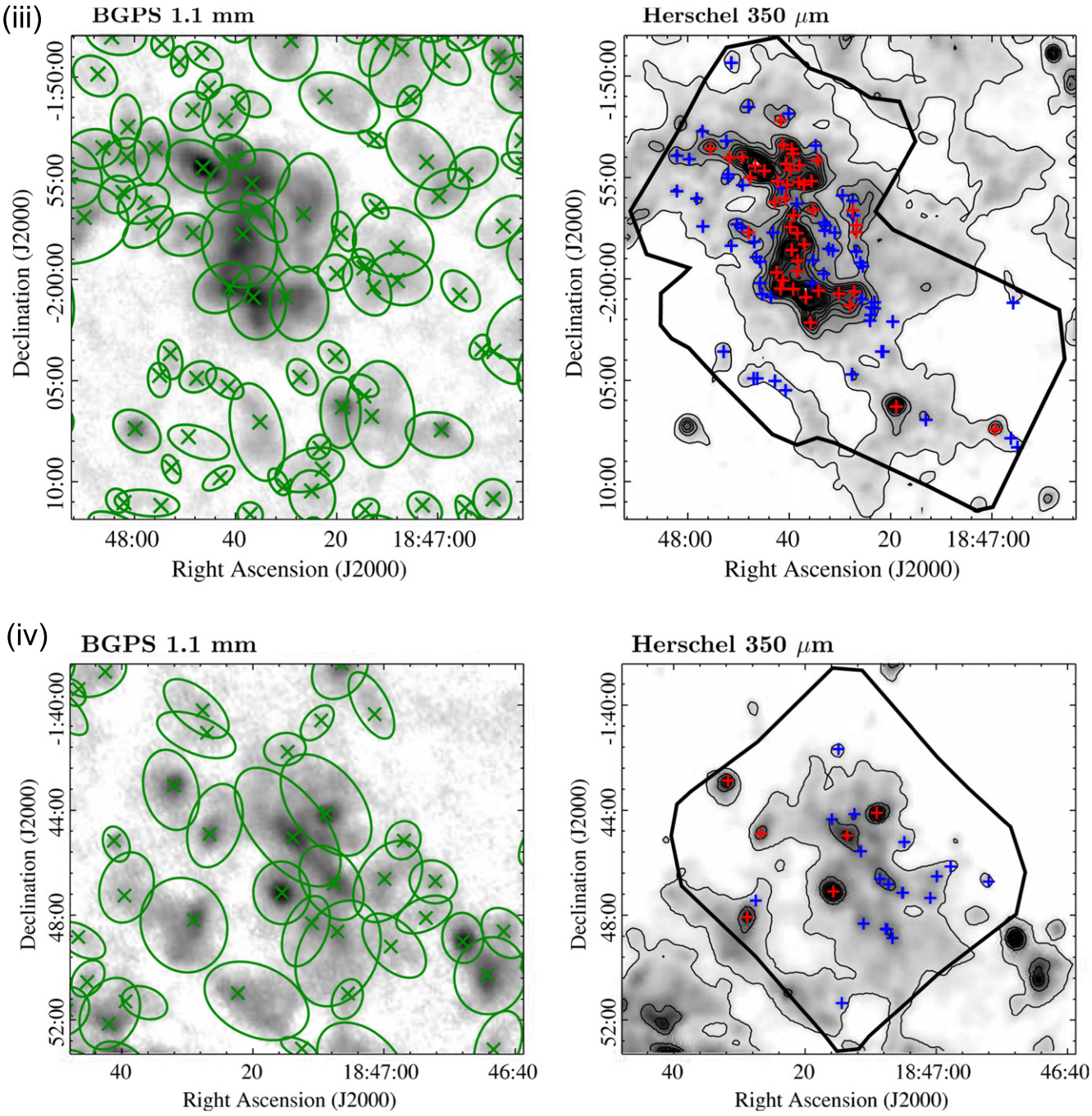

Figure 26. (Continued.)

40″ aperture conversion factors for SHARC-II maps convolved to a resolution of 33″ are shown in the table.

APPENDIX B
SHARC-II MAPS

We present in Figure 25 our complete sample of 107 regions mapped with SHARC-II. For each of them, the image shows gray scale maps with emission contours at 3σ, 6σ, 10σ, 15σ, 30σ, 50σ, and 100σ, with σ the rms noise. The value of σ in units of mJy beam^{-1} is stated below each map. The image also shows the high-resolution sources extracted with *Bolocat*. Red contours represent sources with S/N values above 10 (compact sources) and blue contours sources below this limit (faint sources).

APPENDIX C
Hi-GAL SPIRE IMAGES AT 350 μm *FOR* $l = 30°$

In this section we indicate the locations of the high-resolution sources identified in the 350 μm SHARC-II maps (8.″5 beam size) toward $l = 30°$, and their comparison with structures observed at lower resolution (24.″9) in the corresponding *Herschel*/SPIRE maps at the same wavelength and

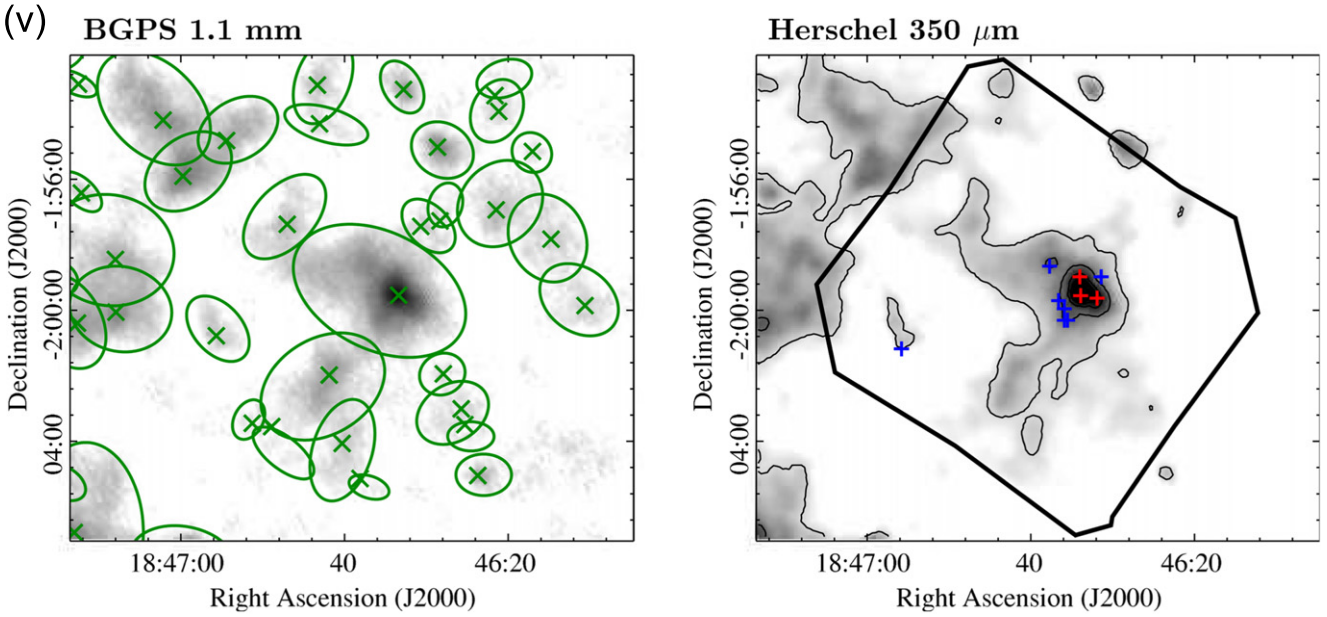

Figure 26. (Continued.)

BGPS maps at 1.1 mm at a resolution of 33″. Figure 26 shows 1.1 mm continuum gray scale maps with green contours representing sources from the BGPS catalog, and *Herschel* gray scale maps with contours representing the emission at 10σ, and increasing steps of 5σ, with $\sigma = 164$ MJy sr^{-1}. The thick black line on each map represent the area covered by the SHARC-II maps, with the name of those maps indicated for each region. Peak positions of detected high-resolution sources from SHARC-II maps are overlaid in red and blue crosses, representing sources with S/N above and below a value of 10, respectively. Most sources with high S/N are well associated with strong emission in the *Herschel* maps, but several of the low S/N sources are not individually identified and they are part of extended background emission detected in *Herschel* maps but not recovered in SHARC-II maps.

REFERENCES

Aguirre, J. E., Ginsburg, A. G., Dunham, M. K., et al. 2011, ApJS, 192, 4
Bally, J., Aguirre, J., Battersby, C., et al. 2010, ApJ, 721, 137
Bally, J., & Zinnecker, H. 2005, AJ, 129, 2281
Battersby, C., Bally, J., Ginsburg, A., et al. 2011, A&A, 535, A128
Battersby, C., Bally, J., Jackson, J. M., et al. 2010, ApJ, 721, 222
Beckwith, S. V. W., & Sargent, A. I. 1991, ApJ, 381, 250
Beelen, A., Cox, P., Benford, D. J., et al. 2006, ApJ, 642, 694
Benjamin, R. A., Churchwell, E., Babler, B. L., et al. 2003, PASP, 115, 953
Bertin, E., & Arnouts, S. 1996, A&AS, 117, 393
Bohlin, R. C., Savage, B. D., & Drake, J. F. 1978, ApJ, 224, 132
Butler, M. J., & Tan, J. C. 2012, ApJ, 754, 5
Carey, S. J., Noriega-Crespo, A., Mizuno, D. R., et al. 2009, PASP, 121, 76
Cesaroni, R., Olmi, L., Walmsley, C. M., Churchwell, E., & Hofner, P. 1994, ApJL, 435, L137
Cesaroni, R., Walmsley, C. M., Koempe, C., & Churchwell, E. 1991, A&A, 252, 278
Churchwell, E., Walmsley, C. M., & Cesaroni, R. 1990, A&AS, 83, 119
Contreras, Y., Schuller, F., Urquhart, J. S., et al. 2013, A&A, 549, A45
Draine, B. T., & Lee, H. M. 1984, ApJ, 285, 89
Dowell, C. D., et al. 2003, Proc. SPIE, 4855, 73
Dunham, M. K., Rosolowsky, E., Evans, N. J., II, et al. 2010, ApJ, 717, 1157
Dunham, M. K., Rosolowsky, E., Evans, N. J., II, Cyganowski, C., & Urquhart, J. S. 2011, ApJ, 741, 110
Egan, M. P., Shipman, R. F., Price, S. D., et al. 1998, ApJL, 494, L199
Elia, D., Molinari, S., Fukui, Y., et al. 2013, ApJ, 772, 45
Ellsworth-Bowers, T. P., Glenn, J., Rosolowsky, E., et al. 2013, ApJ, 770, 39
Ellsworth-Bowers, T. P., Glenn, J., Rosolowsky, E., et al. 2015, ApJ, 799, 29
Evans, N. J., II 1999, ARA&A, 37, 311
Faúndez, S., Bronfman, L., Garay, G., et al. 2004, A&A, 426, 97
Foster, J. B., & Goodman, A. A. 2006, ApJL, 636, L105
Garay, G., & Lizano, S. 1999, PASP, 111, 1049
Ginsburg, A., Glenn, J., Rosolowsky, E., et al. 2013, ApJS, 208, 14
Groesbeck, T. D. 1995, PhD thesis, Caltech
Hatchell, J., & Dunham, M. M. 2009, A&A, 502, 139
Johnstone, D., & Bally, J. 2006, ApJ, 653, 383
Johnstone, D., Matthews, H., & Mitchell, G. F. 2006, ApJ, 639, 259
Klein, R., Posselt, B., Schreyer, K., Forbrich, J., & Henning, T. 2005, ApJS, 161, 361
Kovács, A. 2006, PhD thesis, Caltech
Krugel, E., Densing, R., Nett, H., et al. 1989, A&A, 211, 419
Krumholz, M. R., & McKee, C. F. 2008, Natur, 451, 1082
Longmore, S. N., Rathborne, J., Bastian, N., et al. 2012, ApJ, 746, 117
McKee, C. F., & Ostriker, E. C. 2007, ARA&A, 45, 565
Megeath, S. T., Townsley, L. K., Oey, M. S., & Tieftrunk, A. R. 2008, in Handbook of Star Forming Regions, Vol. 1: The Northern Sky, ed. B. Reipurth (San Francisco, CA: ASP), 264
Molinari, S., Schisano, E., Faustini, F., et al. 2011, A&A, 530, AA133
Molinari, S., Swinyard, B., Bally, J., et al. 2010, PASP, 122, 314
Moore, T. J. T., Bretherton, D. E., Fujiyoshi, T., et al. 2007, MNRAS, 379, 663
Motte, F., Bontemps, S., Schilke, P., Schneider, N., Menten, K. M., & Broguière, D. 2007, A&A, 476, 1243
Motte, F., Zavagno, A., Bontemps, S., et al. 2010, A&A, 518, LL77
Mueller, K. E., Shirley, Y. L., Evans, N. J., II, & Jacobson, H. R. 2002, ApJS, 143, 469e
Ossenkopf, V., & Henning, T. 1994, A&A, 291, 943
Padoan, P., Juvela, M., & Pelkonen, V.-M. 2006, ApJL, 636, L101
Plume, R., Jaffe, D. T., & Evans, N. J., II 1992, ApJS, 78, 505
Ragan, S. E., Henning, T., & Beuther, H. 2013, A&A, 559, AA79
Rathborne, J. M., Jackson, J. M., Chambers, E. T., et al. 2010, ApJ, 715, 310
Rathborne, J. M., Jackson, J. M., & Simon, R. 2006, ApJ, 641, 389
Richards, E. E., Lang, C. C., Trombley, C., & Figer, D. F. 2012, AJ, 144, 89
Rivera-Ingraham, A., Martin, P. G., Polychroni, D., et al. 2013, ApJ, 766, 85
Rosolowsky, E., Dunham, M. K., Ginsburg, A., et al. 2010, ApJS, 188, 123
Schuller, F., Menten, K. M., Contreras, Y., et al. 2009, A&A, 504, 415
Shirley, Y. L., Ellsworth-Bowers, T. P., Svoboda, B., et al. 2013, ApJS, 209, 2

Shirley, Y. L., Evans, N. J., II, Rawlings, J. M. C., & Gregersen, E. M. 2000, ApJS, 131, 249
Shirley, Y. L., Nordhaus, M. K., Grcevich, J. M., et al. 2005, ApJ, 632, 982
Stahler, S. W., Palla, F., & Ho, P. T. P. 2000, Protostars and Planets, 4, 327
Schlingman, W. M., Shirley, Y. L., Schenk, D. E., et al. 2011, ApJS, 195, 14
Simon, R., Jackson, J. M., Rathborne, J. M., & Chambers, E. T. 2006, ApJ, 639, 227
Tan, J. C., Beltran, M. T., Caselli, P., et al. 2014, arXiv:1402.0919
Traficante, A., Calzoletti, L., Veneziani, M., et al. 2011, MNRAS, 416, 2932
Urquhart, J. S., Moore, T. J. T., Schuller, F., et al. 2013, MNRAS, 431, 1752
Wienen, M., Wyrowski, F., Schuller, F., et al. 2012, A&A, 544, A146
Williams, J. P., Blitz, L., & McKee, C. F. 2000, Protostars and Planets, 4, 97
Williams, J. P., de Geus, E. J., & Blitz, L. 1994, ApJ, 428, 693
Wright, E. L., Eisenhardt, P. R. M., Mainzer, A. K., et al. 2010, AJ, 140 1868
Wu, J., Dunham, M. M., Evans, N. J., II, Bourke, T. L., & Young, C. H. 2007, AJ, 133, 1560
Wynn-Williams, C. G., Becklin, E. E., & Neugebauer, G. 1972, MNRAS, 160, 1
Zinnecker, H., & Yorke, H. W. 2007, ARA&A, 45, 481